



Delft University of Technology

Tidal-flat reclamation aggravates potential risk from storm impacts

Zhang, Min; Dai, Zhijun; Bouma, Tjeerd J.; Bricker, Jeremy; Townend, Ian; Wen, Jiahong; Zhao, Tongtiegang; Cai, Huayang

DOI

[10.1016/j.coastaleng.2021.103868](https://doi.org/10.1016/j.coastaleng.2021.103868)

Publication date

2021

Document Version

Accepted author manuscript

Published in

Coastal Engineering

Citation (APA)

Zhang, M., Dai, Z., Bouma, T. J., Bricker, J., Townend, I., Wen, J., Zhao, T., & Cai, H. (2021). Tidal-flat reclamation aggravates potential risk from storm impacts. *Coastal Engineering*, 166, Article 103868. <https://doi.org/10.1016/j.coastaleng.2021.103868>

Important note

To cite this publication, please use the final published version (if applicable). Please check the document version above.

Copyright

Other than for strictly personal use, it is not permitted to download, forward or distribute the text or part of it, without the consent of the author(s) and/or copyright holder(s), unless the work is under an open content license such as Creative Commons.

Takedown policy

Please contact us and provide details if you believe this document breaches copyrights. We will remove access to the work immediately and investigate your claim.

1 **Tidal-flat reclamation aggravates potential risk from storm impacts**

2 Min Zhang^{a,b,c}, Zhijun Dai^c, Tjeerd J. Bouma^b, Jeremy Bricker^d, Ian Townend^e,
3 Jiahong Wen^a, Tongtiegang Zhao^f and Huayang Cai^{g,*}

4 ^aSchool of Environmental and Geographical Sciences, Shanghai Normal University,
5 200234, Shanghai, China

6 ^bDepartment of Estuarine and Delta Systems, Royal Netherlands Institute for Sea
7 Research, 4400 AC, Yerseke, the Netherlands

8 ^cState Key Laboratory of Estuary and Coastal Research, East China Normal University,
9 200062, Shanghai, China

10 ^dDepartment of Hydraulic Engineering, Delft University of Technology, 2628 CN, Delft,
11 the Netherlands

12 ^eSchool of Ocean and Earth Sciences, University of Southampton, SO17 1BJ,
13 Southampton, UK

14 ^fSchool of Civil Engineering, Sun Yat-sen University, 519082, Zhuhai, China

15 ^gSouthern Marine Science and Engineering Guangdong Laboratory (Zhuhai)/ School of
16 Marine Engineering and Technology, Sun Yat-sen University, 519082, Zhuhai, China

17 *Corresponding author: caihy7@mail.sysu.edu.cn (H.Y. Cai)

18

19 **Abstract**

20 A better understanding of how tidal-flat reclamation changes the flood hazard is critical
21 for climate-proofing coastal flood defense design of heavily urbanized areas. Since the
22 1950s, large-scale reclamation has been performed along the Shanghai coast, China, to
23 fulfill the land demands of city expansion. We now show that the loss of tidal flats may
24 have resulted in harmful impacts of coastal storm flooding. Using the foreshore profiles
25 measured before and after reclamation (i.e., wide vs. narrow tidal flat), we determined
26 the long-term changes in flood risk using a numerical model that combines extreme
27 tidal level and wave overtopping analysis. Results show that wide tidal flats in front of
28 a seawall provide efficient wave damping even during extreme water levels.
29 Reclamation of these tidal flats substantially increased wave heights and
30 correspondingly reduced the return period of a specific storm. As a result, estimates of
31 overtopping are aggravated by more than 80% for the varying return periods examined.
32 It is concluded that the disasters of coastal flooding after the 1997 tidal-flat reclamation

33 in Hangzhou Bay, China are a consequence of both anthropogenic and natural activities.
34 Moreover, our model calculations provide an equation describing the equivalent dike
35 height needed to compensate for the loss of every km tidal flat of a certain elevation,
36 and vice versa. For example, for every km of tidal flat ranging from high marsh to bare
37 tidal flat that is being regained, the dike can be lowered by 0.84 m to 0.67 m, when
38 designing for a 1 in 200 years storm event. Overall, we suggest that wide tidal flats are
39 ideally restored in front of dikes, and that when tidal areas are reclaimed, the seawall
40 height is raised as part of the intertidal reclamation procedure. Using such an equivalent
41 protection standard is relevant to designing hybrid flood defense system worldwide.

42

43 **Keywords:** Reclamations, Extreme value analysis, Storm flooding, Joint probability
44 analysis, Equivalent protection standard

45

46 **1 Introduction**

47 Most developing countries with a high population density in Asia, including China,
48 Vietnam, Bangladesh, and the Philippines, primarily rely on seawalls for coastal storm
49 protection (Temmerman et al., 2013; Barbier, 2015). Unfortunately, the natural storm
50 flood mitigation functions of tidal flats (i.e., here refer to both unvegetated mudflat and
51 saltmarshes) have been underappreciated (Möller et al., 2014). Since the middle of the
52 last century, many of these countries have reclaimed large littoral areas for land
53 demands (Bi et al., 2012; Barbier, 2015). The newly reclaimed polders that have been
54 moved further seaward are generally low-lying, and thus highly sensitive to storm
55 impacts. In order to address this issue, China, for instance, had constructed long, hard-
56 engineered defenses of approximately 14,000 km length in total along the 34,000 km-
57 long coastlines to protect its coastal population of roughly 600 million (Liu et al., 2019).
58 The benefit of hard-engineered structures in mitigating economic loss and casualty is
59 universally recognized. However, environmental changes of sea-level rise, land
60 subsidence, and record-breaking extreme storm events are eroding the seawall's
61 protective ability (Temmerman et al., 2013). Maintenance costs are hence expected to
62 rise with time (Liu et al., 2019). Tidal flats are increasingly recognized as “recumbent
63 seawalls”, providing long-term protection to the conventional hard-engineered defenses
64 (Willemsen et al. 2020). These natural interfaces with the sea have an inherent resilience
65 against sea-level rise (Kirwan et al., 2016) and hence, in contrast to human-constructed
66 defenses, do not need structural maintenance, and further provide valuable ecosystem

67 services that vertical seawalls do not offer (Reed et al., 2018).

68 From all intertidal ecosystems, vegetated foreshores are most efficient in
69 attenuating waves due to their highly elevated position in the intertidal zone (Bouma et
70 al. 2014). Therefore, vegetated foreshores, like saltmarshes (Möller et al., 2014) and
71 mangrove forests (Menéndez et al., 2018), are well recognized as ecosystem-based
72 flood protection to reduce storm impacts. Wave mitigation by vegetated foreshores
73 depends both on plant traits like shoot stiffness and shoot biomass (Bouma et al., 2005;
74 2010), stem height, stem diameter, and stem density (Reed et al., 2018), as well as
75 ecosystem traits like marsh width (Willemsen et al., 2020). Even if plant stems break
76 during an extreme storm or are absent, tidal foreshores may still attenuate waves by
77 morphological effects like topographic slopes (Loder et al., 2009; Vuik et al., 2018),
78 bottom friction (Möller et al., 2014), and depth-induced wave breaking (Altomare et al.,
79 2016). Translating this kind of knowledge on wave attenuation to designing hybrid
80 flood defense systems, which consists of a seawall behind a tidal flat, requires
81 numerical models (Vuik et al., 2018). In this study, we aim to integrate the effect of
82 extreme water levels with storm wave run-up into a single long-term modeling effort to
83 quantify how the flood risks of a hybrid flood defense system changes after land
84 reclamation. That is, we model under extreme storm conditions, how wave loading and
85 wave overtopping changes in response to reclamation of tidal areas.

86 Our study site is the Fengxian Coast, located on the northern bank of Hangzhou
87 Bay, China. Since the 1950s, a large-scale coastal embankment program has been
88 implemented, aiming to improve flood defense and navigation (Xie et al., 2017; Zhang
89 et al., 2018a). At the beginning, embankments only occurred above the high-water level
90 (i.e., high marsh area); however, they were gradually extended onto the intertidal zone
91 (i.e., including low marshes and bare tidal flats), and now reclamation is being
92 performed beyond the low-water level at the -5 m sub-tidal zone to fulfill the increasing
93 land demand (Zhang et al., 2018a) (Fig. 1b). Embankments above the high-water level
94 are believed to be beneficial for flood mitigation (Kundzewicz et al., 2019; Wang et al.,
95 2012). However, little is known about the actual consequences of intertidal reclamation
96 for coastal flood safety and if such measures could reduce or magnify coastal flood risk
97 due to the change of wave run-ups. Moreover, in recent years the Fengxian Coast has
98 changed from being an area of accreting to eroding (Xie et al., 2017), which will lead
99 to an even lower and narrower foreshore at the toe of the seawall in the future. It is
100 reported that the coastal embankments in Bangladesh in the intertidal zone have not

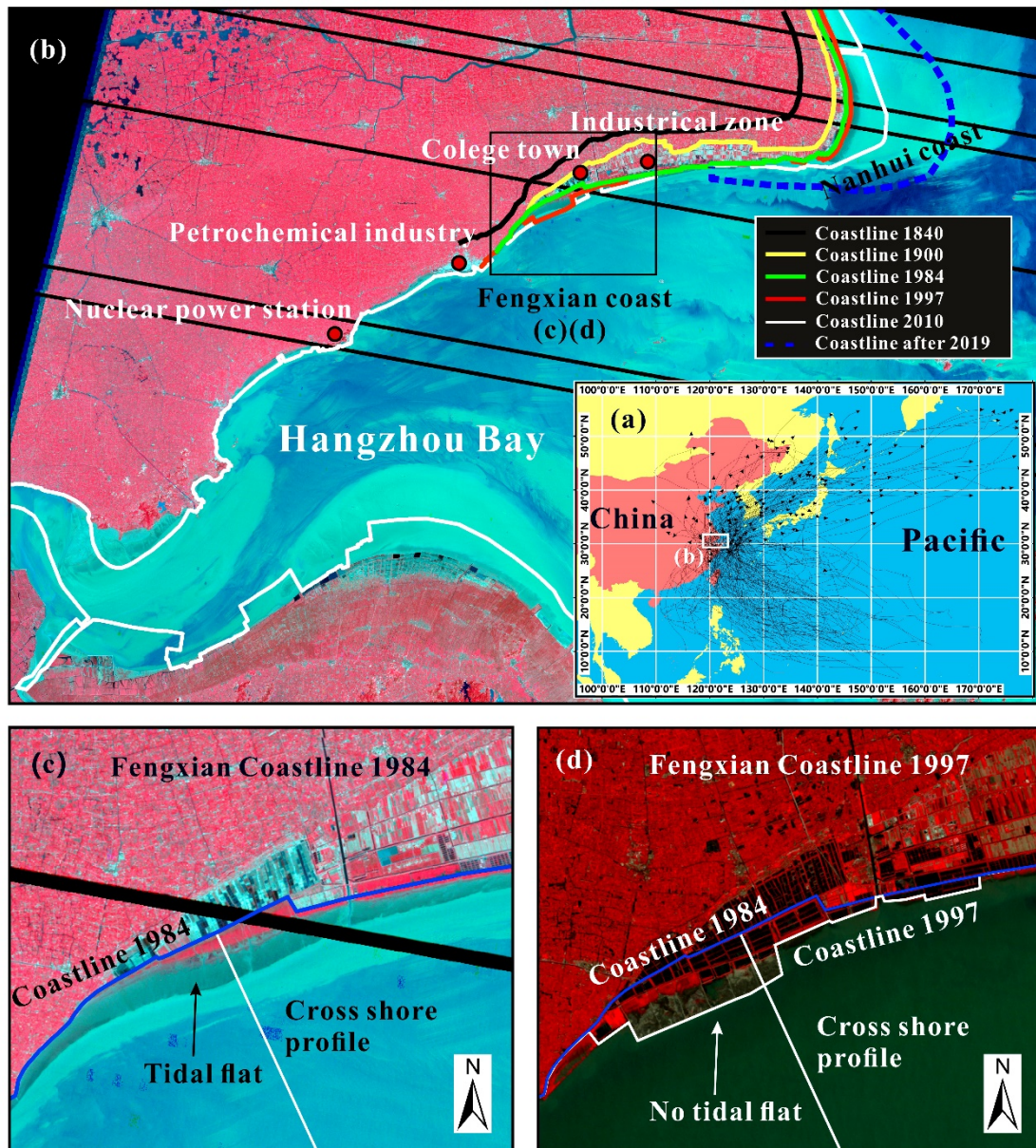
101 always made a positive contribution to flood mitigation (Adnan et al., 2019). Similarly,
102 it is questionable whether the substantial inter- and sub-tidal embankments have
103 reduced flooding risk along the Hangzhou Bay. Therefore, there is a need for a better
104 understanding of the role of tidal flat in helping to mitigate the flood hazard.

105 In this study, we determine the long-term changes in flood risk using a numerical
106 model that combines extreme tidal levels with wave overtopping analysis, using the
107 foreshore profiles measured before and after reclamation (i.e., wide vs. narrow tidal flat)
108 at the Fengxian Coast. That is, we primarily assess the impacts of reclamation on flood
109 risks by comparing the wave impact on the seawall behind the wide high marsh tidal
110 flat as present in 1984 versus the seawall behind the narrower bare tidal flat as formed
111 after the reclamation that had taken place between 1984 and 1997 (immediately prior
112 to the No. 9711 typhoon event, <http://typhoon.zjwater.gov.cn/>, accessed on 15 August,
113 2019). These analyses are done on a selected length of the Fengxian Coast, where
114 crucial industries and a college town suffered severe coastal flooding during the No.
115 9711 typhoon event, resulting in approximately \$5.5 billion direct damages (Wang et
116 al., 2012). Particularly, we explored whether reclamations had intensified wave
117 overtopping and increased damage of the No. 9711 event, and to what extent the damage
118 is due to human interventions. A quantitative relationship between the width of
119 intertidal flat (in the horizontal scale) and the height of seawall (in the vertical scale) on
120 equivalent flood protection has been derived to inform the discussion on the non-
121 stationary seawall-foreshore redesign, and how this contributes to or detracts from
122 coastal flood protection.

123 **2 Study area and foreshore bathymetric measurements**

124 The Fengxian Coast is situated on the northern bank of Hangzhou Bay, the largest
125 embayment of China, and on the southern bank of Shanghai Municipality, which hosts
126 the largest economy in China (Fig. 1). It is a region of high importance, having crucial
127 nuclear energy infrastructure, petrochemical industry, and a college town (Fig. 1b). The
128 closest tide gauge station shows that storm surges influencing the Fengxian Coast
129 propagate primarily from Hangzhou Bay, which is a typical funnel-shaped estuary
130 dominated by tides. The semi-diurnal mesotide is approximately in the range of 3 - 4 m
131 at the entrance of the Fengxian Coast, and increases gradually upstream to reach a
132 maximum of approximately 5 - 7 m due to the massive bay convergence and broad fetch
133 condition (Xie et al., 2017). This region serves as a location for flood risk studies
134 because of its substantial tidal flat loss and severe coastal storm flooding in history.

135 Coastal reclamation implemented around Shanghai has a long history (Fig. 1b).
136 Since the 1950s, coastal embankments have been built to improve flood defense and
137 navigation. Unforeseen, the Fengxian Coast has been increasingly flooded, exacerbated
138 by sea defense breaching and overtopping. The most notable example of this is the No.
139 9711 flooding on 18 August 1997. During this prolonged event, more than 10 km of the
140 seawall was overtopped or breached by a 1 in 200-yr extreme water level coupled with
141 6 m high waves (see Supplementary Fig. S1, S2). The flooding extended up to 5 km
142 inland and a maxima depth of 1.2 m due to the low-lying, flat nature of the polders.
143 Hence, the intertidal profile immediately prior to the No. 9711 typhoon event,
144 representing the pre-typhoon conditions, and a much earlier intertidal profile before
145 large-scale reclamations in 1984, are employed to detect the effects of reclamation on
146 flood risk aggravation.

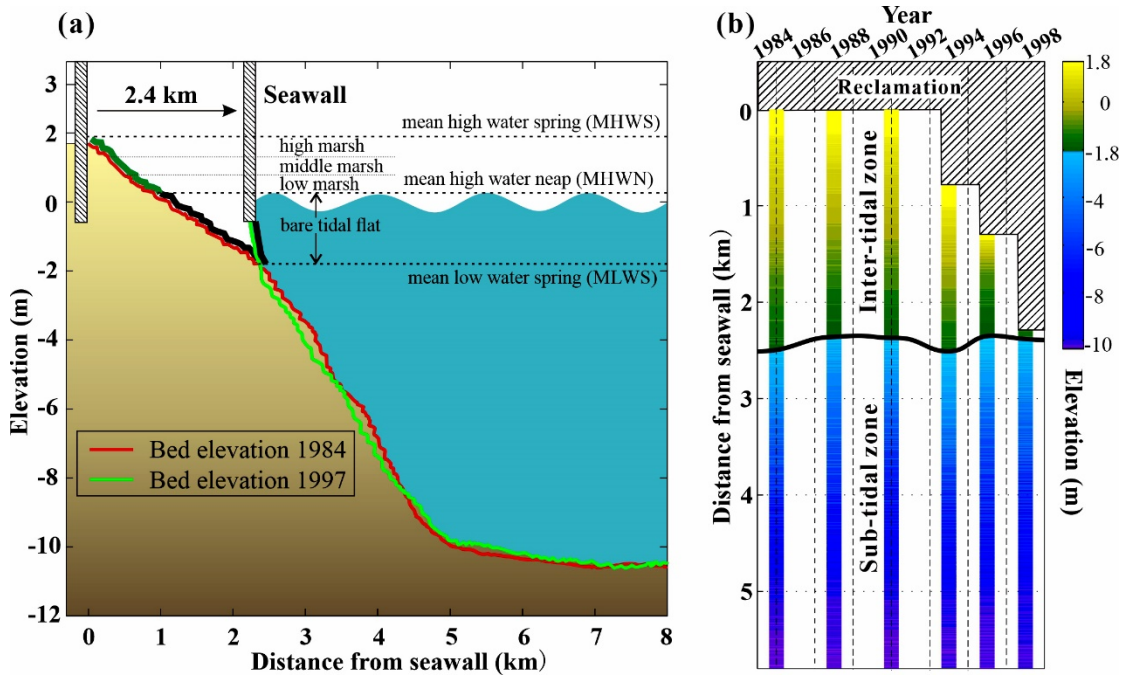


147

148 Fig. 1. Archived satellite images showing the history of the study area. (a) The tracks
 149 of typhoon events affecting Shanghai during the past 40 years, (b) the historical
 150 embankments along the Fengxian Coast and Hangzhou Bay from 1840 to 2010, the area
 151 is occupied by existing operational nuclear energy assets, petrochemical industries, and
 152 college town, (c, d) detailed map showing the location of seawalls along the Fengxian
 153 Coast in the year of 1984 and 1997, the land between the two sets of seawalls denote
 154 the reclaimed area.

155 Since the start of reclamation, intertidal profiles had been measured frequently on
 156 the Fengxian Coast (Fig. 2). These measurements are part of the Flood Defense Safety
 157 led by the Chinese State of Ocean Administration, the governmental subdivision in
 158 charge of flood-risk management. A littoral wide intertidal section (slope of

159 approximately 1:700) was present in the 1984 profile, which had been reclaimed in the
 160 years 1993, 1995, and 1997, with the polder marching seaward by 2.4 km (Fig. 2). The
 161 seawall foundation of 1997 is almost located at the lower margin of the bare tidal flat
 162 of 1984, which is in accordance with typical reclamation procedures in China, leaving
 163 the toe of the seawall almost uncovered by mud at time prior to the No. 9711 typhoon
 164 event. The pre- and post-reclamation profiles are used to determine whether the changes
 165 in the tidal flat morphology could influence wave overtopping under storm conditions.



166
 167 Fig. 2. Morphodynamics of the cross-shore profiles. (a) Schematic representation of
 168 seawall-foreshore change with marks indicating ocean parameters of mean high water
 169 spring (MHWS), mean low water spring (MLWS), mean high water neap (MHWN),
 170 and foreshore division of high marsh (1.3 ~ 1.8 m), middle marsh (0.8~1.3 m), low
 171 marsh (0.3 ~ 0.8 m) and bare tidal flat (-1.8 ~ 0.3 m). The location of cross-shore
 172 profiles measurements are shown in Fig. 1c and d. (b) Detailed bed elevation
 173 measurements between 1984 and 1997, including the hard boundary of seawall toe
 174 position and the position of MLWS (the solid black line of -1.8 m). The change of
 175 seawall position denotes the reclamation procedures occurring in 1993, 1995, and 1997.
 176 The distance between seawall and MLWS is the intertidal zone, where marshes are
 177 believed to grow above 0.3 m.

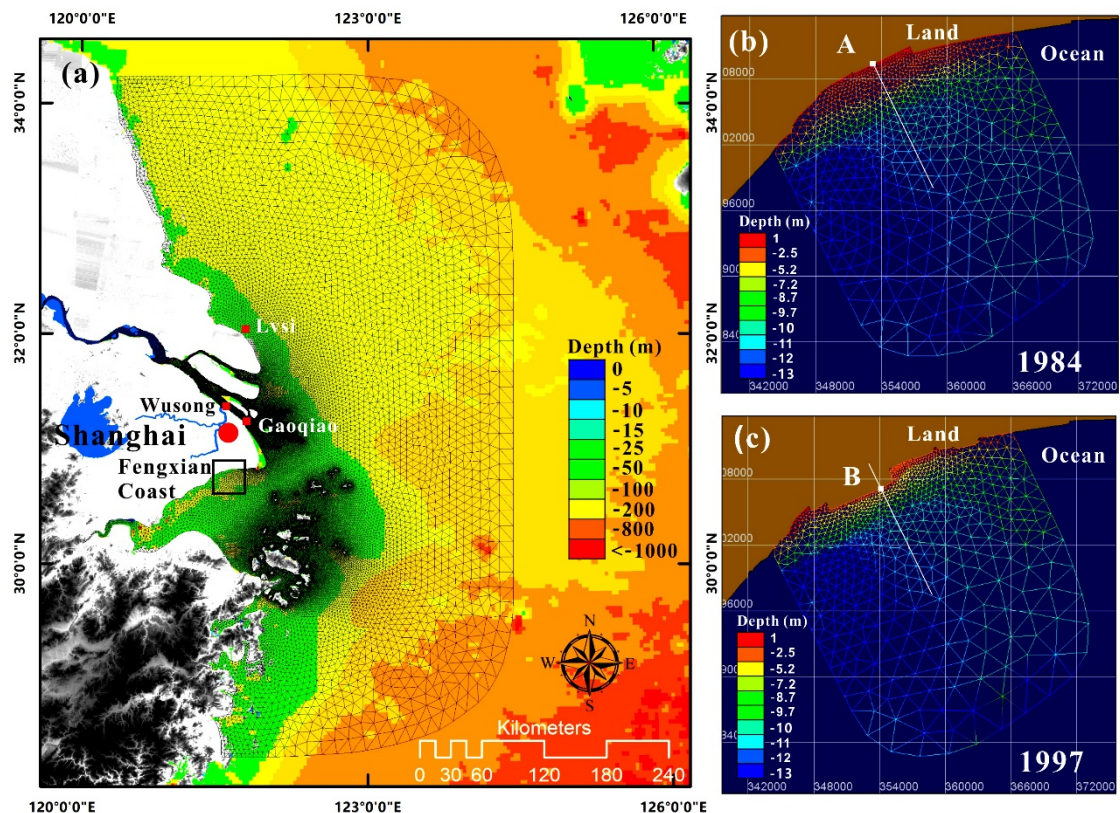
178 **3 Methodology**

179 The investigation into the impacts of intertidal reclamations on aggravated risks
 180 from storm surges have been addressed in the following three steps: (1) a framework of

181 numerical models hindcasting tides and waves with improved accuracy is used to
 182 downscale the offshore sea states to those at the toe of the seawall; (2) the outputs of
 183 tidal levels (*TLs*) and significant wave heights (*SWHs*) of independent storms are used
 184 for the extreme value analysis, and the resulted marginal distributions are further fed
 185 into the joint probability model for overtopping estimation using the method by Tuan
 186 and Oumeraci (2010); and (3) the different effects under the adopted bathymetry
 187 profiles before and after reclamation in 1984 and 1997 are compared.

188 3.1 Wave and surge models

189 The long-term tides and storm surges are generated using the coupled TELEMAC-
 190 TOMAWAC modules to capture the wave-current interactions (Zhang et al., 2018a).
 191 The full, two-dimensional primitive equations of Navier Stokes and the balance
 192 equations of wave action density spectrum for both deep and shallow water physics are
 193 solved using the finite difference method (Janin et al., 1992). The computational
 194 domain, shown in Fig. 3a, encompasses the entire Yangtze Estuary and Hangzhou Bay
 195 and a portion of the nearby coastal regions. The domain is extended to ensure a
 196 sufficient fetch for wave simulation, so that the development of storm swells in the deep
 197 ocean and the propagating with tides to the nearshores are captured (Zhang et al., 2018a).
 198 An appropriate simulation of tides and swells propagation to nearshore is crucial for a
 199 high-accuracy simulation of wave runups at the toe of seawall.



201 Fig. 3. Maps of the modeling domain. (a) Regional domain of Yangtze-Hangzhou Bay
202 model for the tide and swell simulation, and (b, c) local domain of the Fengxian Coast
203 model for the wave simulation with the applied morphology profile of 1984 and 1997
204 bathymetry, respectively. The solid white lines indicate the location of cross-shore
205 profiles the same as shown in Fig. 1c, d.

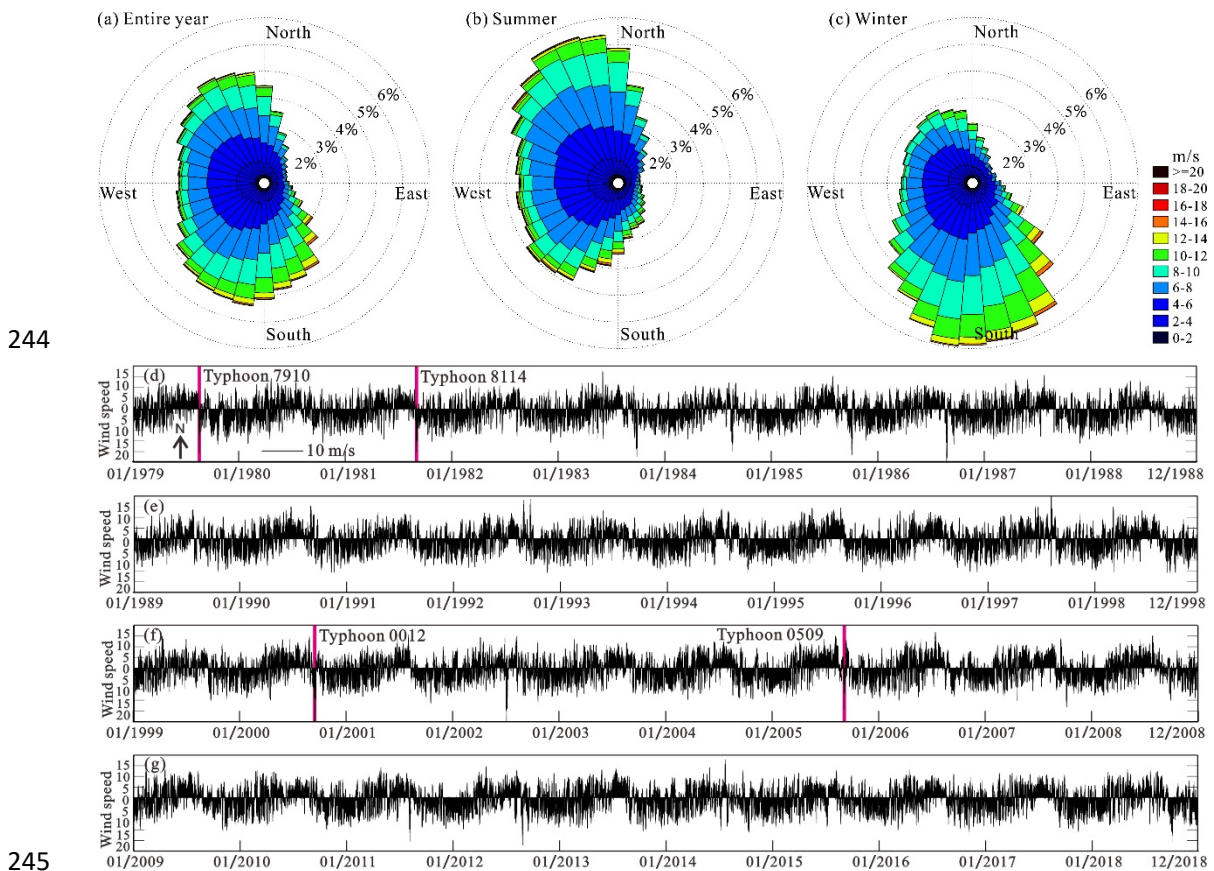
206 In order to obtain the long-term nearshore waves, two sets of local wave models
207 embedded with 1984 and 1997 bathymetries, covering the Fengxian Coast (Fig. 3b, c),
208 are configured with TOMAWAC module (EDF, 2011), and cascading to the upper-
209 level Yangtze-Hangzhou Bay model. For the local wind-wave simulations, wave
210 energy dissipation mechanisms, including bottom friction, wave breaking, and white
211 capping, are triggered. JONSWAP-type bottom friction and depth-induced wave
212 breaking are used. The spectral frequency is discretized by 30 frequencies, with a
213 minimum frequency of 0.055 Hz, increasing equidistantly at an interval of 0.03 Hz. The
214 bathymetries are also delineated with unstructured irregular triangular meshes, with the
215 edges aligned with the 1984 and 1997 coastlines, respectively. Both local wave models
216 are run with the same meteorological and oceanic forces, i.e., at the sea surface
217 boundary, temporally variable and spatially uniform 10 m height wind force, obtained
218 from field measurements is used; at the lateral sea boundary, water levels and wave
219 spectra extracted from the regional domain model are interpolated onto the seaward
220 boundary of the TOMAWAC model to consider swell and wave propagation from the
221 deep ocean.

222 After the bathymetries of the meshes are corrected to the consistent datum of
223 Huanghai 1985, the depths are modified to account for sea-level rise (SLR), which has
224 been shown to have some influences on nearshore wind-wave generation (Chini and
225 Stansby, 2012). The present simulation assumed a linear SLR rate of 3.5 mm/yr over
226 the past 40 years. Early estimates of the SLR for the region of the East China Sea ranged
227 from 2.1 to 2.5 mm/yr (Shi et al., 2000), whereas more recent studies (post-1990), based
228 on a satellite altimeter, suggested a higher rate of 5 - 6 mm/yr (Chini and Stansby, 2012).

229 **3.2 Data sources used to set-up model**

230 To drive the large-scale Yangtze-Hangzhou Bay model, long-term astronomical
231 tide and atmosphere (e.g., wind and pressure) data for the past 40 years are derived
232 through the TOPEX/POSEIDON global ocean tidal model (TPXO,
233 <http://volkov.oce.orst.edu/tides>, accessed on 15 August 2019) calculation and European
234 Centre for Medium-Range Weather Forecasts (ECMWF, <http://www.ecmwf.int/>,

235 accessed on 15 August 2019) reanalysis, respectively. The tidal amplitudes at the ocean
 236 boundary are forced with harmonic compositing of eight primary, two long-period, and
 237 three non-linear constituents provided by TPXO (Zhang et al., 2018a). The temporal
 238 and spatial resolution for the wind and pressure field derived from ECMWF is 3 h and
 239 12.5 km, respectively. Such high-resolution data are a proper source to drive the ocean
 240 model over a large area because the forces imposed on the Yangtze-Hangzhou Bay
 241 model encompass distinct pressure gradients and heat capacity contrasts from the
 242 typhoon center to the margin, resulting in rapidly varying wind and pressure fields (Dee
 243 et al., 2011).



245
 246 Fig. 4. Meteorological data of wind observed uninterrupted during 1979 - 2018 recorded
 247 by the Fengxian Observation Station ($E121.45^{\circ}$, $N30.93^{\circ}$). (a, b, c) The wind rose of the
 248 entire year, the summer (May - October) and winter (November - April) periods. (d, e,
 249 f, g) The 6-hourly recorded wind magnitudes and directions from 1979 - 2018.

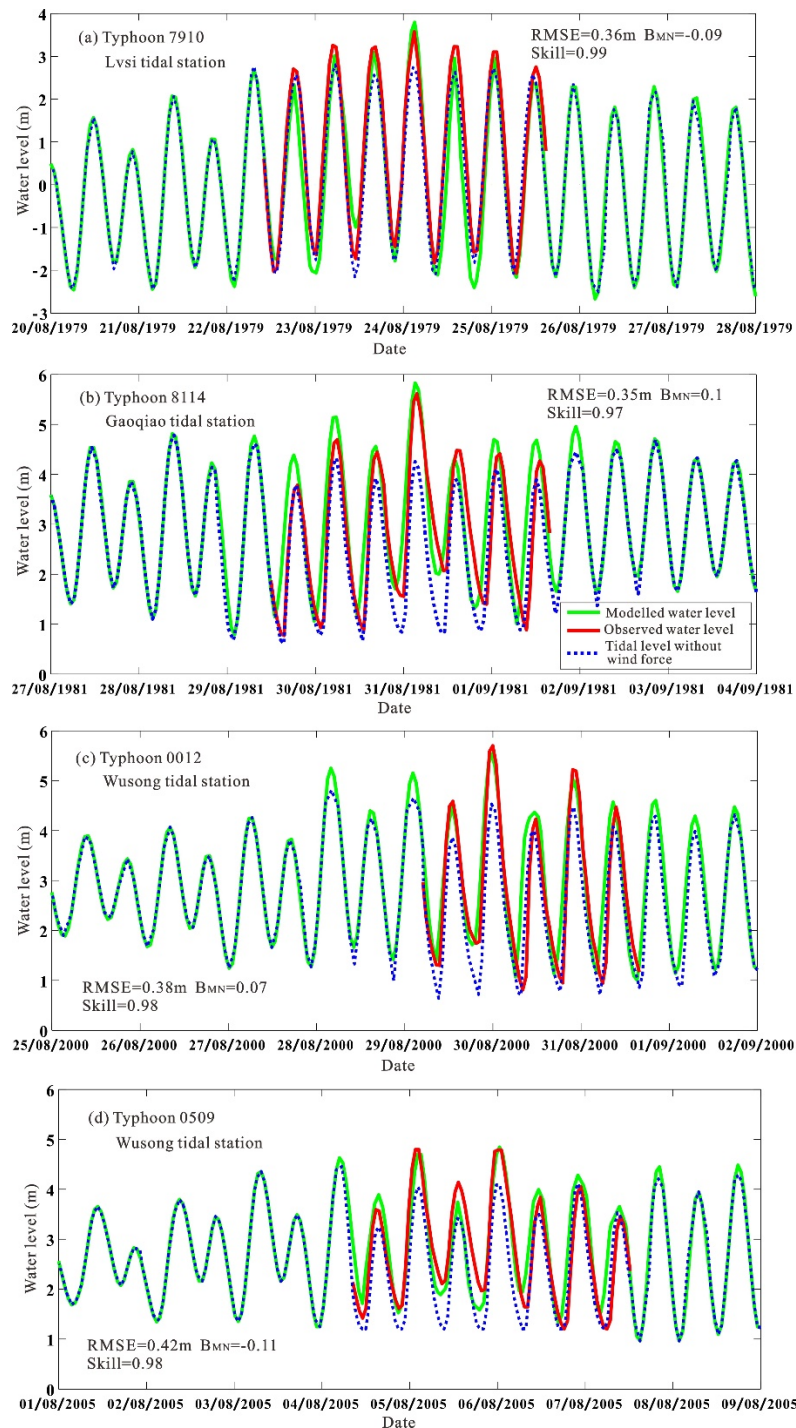
250 In addition to the meteorological data from ECMWF, a 40-yr uninterrupted wind
 251 data recorded every 6 hours between 1979 - 2018 by the Fengxian Observation Station
 252 ($E121.45^{\circ}$, $N30.93^{\circ}$, established in 1961) are collected from the Shanghai
 253 Meteorological Bureau, and is presented in Fig. 4d, e, f, and g. Seasonal variability in
 254 wind directions is clearly observed. They are used to force both sets of local models,

255 i.e., the morphologies of 1984 and 1997, respectively. By setting a high wind threshold
256 of 15 m/s, the peak-over-threshold analysis (Méndez et al., 2006) performed on the
257 wind data above the given threshold identified 270 typhoon events that had hit Shanghai
258 during the past 40 years (Fig. 1a).

259 Other observation data used in the model include seabed bathymetries and
260 hydrologic station records. The archived daily river discharge measured at the Datong
261 station (1981 - 2018) is imposed on the river boundary to capture the signal of abrupt
262 releases of discharges from the Changjiang River catchment. The depth information of
263 the mesh is defined by the amalgamation of heterogeneous databases, including the
264 General Bathymetric Charts of the Oceans (GEBCO, <https://www.gebco.net>, accessed
265 on 15 August 2019) dataset, covering the continental shelf area, the 2007 and 2008
266 navigation charts collected for the Yangtze River channel, the river mouth and the bar
267 area. These data are all interpolated and corrected relative to the mean sea level of the
268 Huanghai 1985 datum in ArcGIS software.

269 **3.3 Model performance**

270 Because the hindcast of the 40 years storm tide simulation is substantial, only
271 selected periods are used for simulation-measurement comparisons. Four periods of
272 simulated and observed water levels at tidal stations of Lvsi, Gaoqio, and Wusong (see
273 their locations in Fig. 3a) affected by devastating typhoons are illustrated in Fig. 5.
274 These storms were reported to have caused the most substantial economic losses for
275 Shanghai over the past half-century (Wang et al., 2012). Typhoon 7910 in August 1979
276 and Typhoon 8114 in August 1981 are used for calibration, while Typhoon 0012 in
277 August 2000 and Typhoon 0509 in August 2005 are used for validation (see Fig. 4d, e,
278 f, and g for corresponding wind forces). In order to quantify the model's performance,
279 the correlation coefficients of root-mean-square error (RMSE), mean-normalized bias
280 (B_{MN}), and skill value between simulations and measurements are evaluated, as
281 presented in Fig. 5. The RMSE, B_{MN} , and skill values of the measurements are fairly
282 consistent with the simulations with means of 0.38 m, 0.09, and 0.99, respectively. The
283 maximum RMSE and B_{MN} values are 0.42 m and -0.11 (negative means
284 underprediction), respectively, at the Wusong station for Typhoon 0509, but the model's
285 skill value reached 0.98, indicating the reasonable accuracy of the model performance.



286

287 Fig. 5. The comparison of modeled (green line) and observed (red line) water levels at
 288 tidal stations of Lvsi, Gaoqiao, and Wusong (see Fig. 3a) during typical typhoons of (a)
 289 7910, (b) 8114, (c) 0012, and (d) 0509. The blue dot lines show the tidal level without
 290 considering the typhoon wind forces.

291 Based on the above-mentioned model calibration and validation procedures, some
 292 common modeling parameters are determined, including the hydrodynamic time step
 293 of 180 s, the horizontal diffusion viscosity coefficient of $0.1 \text{ kgm}^{-1}\text{s}^{-1}$. A linearly
 294 increasing wind friction coefficient (i.e., from 0.00125 for 7 m/s wind speed to 0.0025

295 for 25 m/s wind speed) is applied in order to resolve the error of underestimated peak
 296 typhoon wind speed from ECMWF (Dee et al., 2011). A Nikuradse bottom frictional
 297 coefficient of $N = 0.05 \pm 0.02$ m is used, based on the Manning values typically used
 298 for tidal marshes in typhoon conditions (Möller et al., 2014; Vuik et al., 2016). For the
 299 bare tidal flats, $N = 0.001$ m is applied. For detailed descriptions of the model's
 300 configuration and calibration around the Yangtze Estuary and Hangzhou Bay, readers
 301 can refer to our previous publications, such as Zhang et al. (2018a; 2019).

302 **3.4 Extreme value analysis**

303 The hourly-simulated *TLs* and *SWHs* during typhoon periods are extracted and
 304 subjected to extreme value analysis by fitting to the appropriate marginal distributions,
 305 i.e., Normal, Gamma, Weibull, and GEV (generalized extreme value) (Niroomandi et
 306 al., 2018). Statistics of the Chi-Square test for the theoretical distributions indicating
 307 the best choice is GEV distribution (see Supplementary Table S1). Firstly, the
 308 stationarity GEV distribution is used to model the different behavior of extremes with
 309 three parameters $\theta = (\mu, \varepsilon, \sigma)$, representing the location, shape, and scale parameters,
 310 respectively. The cumulative distribution function of stationarity GEV is given by
 311 (Chini and Stansby, 2012):

$$312 \quad F(z) = \exp\{-[1 + \varepsilon(\frac{z-\mu}{\sigma})]^{-1/\varepsilon}\}, \quad \varepsilon\left(\frac{\mu-z}{\sigma}\right) < 1, \quad (1)$$

313 where z is the variable of *TLs* or *SWHs*. The Mann-Kendall and likelihood ratio
 314 estimation are then performed to test the time-series trends (Cheng et al., 2014). If the
 315 trend is significant, a linear function of parameter μ is included in order to take into
 316 account non-stationarity:

$$317 \quad \mu = \mu_0 + \mu_1 t, \quad (2)$$

318 where t is the time in years, μ_0 is a constant and μ_1 is the linear trend. In this way,
 319 GEV is extended with four parameters $\theta = (\mu_0, \mu_1, \varepsilon, \sigma)$ to predict the future extremal
 320 levels in a non-stationarity form, e.g., $t=0$ for 1979, $t=40$ for 2019 and $t=121$ for 2100.
 321 A framework combining Differential Evolution Markov Chain (DE-MC) and Bayesian
 322 inference (Cheng et al., 2014) is used to obtain the uncertainty bounds (95% quantile)
 323 of the ensemble of estimated return levels, taking into account the uncertainty in all
 324 model parameters for both stationarity $(\mu, \varepsilon, \sigma)$ and non-stationarity $(\mu_0, \mu_1, \varepsilon, \sigma)$.
 325 Finally, the return period (T), representing an event that has a $1/T$ chance of occurrence
 326 in any given year, is estimated by the following formula:

$$327 \quad T(z) = \frac{1}{1-F(z)}. \quad (3)$$

328 For each set of bathymetries, the return periods of *TLs*, $F(w)$, and *SWHs*, $F(s)$,
329 are estimated by Eq. (3), denoted by $T(w)$ and $T(s)$, respectively.

330 One primary concern of the extreme value analysis lies in the application of
331 monthly maxima data, thus ignoring other essential values during the month
332 (Niroomandi et al., 2018). However, most typhoons hit Shanghai only in summer, i.e.,
333 June to October (Wang et al., 2012; 2019). In this study, the peak-over-threshold (*POT*)
334 method, combined with the block maxima, is used to reduce this limitation by
335 identifying independent storms (Méndez et al., 2006). The wind speeds above a
336 threshold of 15 m/s and a successive time span maximum of 3 days (regarded as a block)
337 are used to guarantee the independency between consecutive storms. The block maxima
338 method is then used to extract the independent maxima for each storm. These criteria
339 enable the division of the entire data into non-overlapping periods of individual storms
340 as blocks and the selection of the maximum value from each block; therefore, it is
341 deemed adequate to perform extreme value analysis. As a result, there are samples of
342 270 extreme values used to fit the GEV distribution for the long-term 40-yr study.

343 **3.5 Copulas joint probability analysis**

344 Since *TLs* and *SWHs* are rarely statistically independent, the joint probability of
345 multivariate analysis (i.e., the Copulas) is used to calculate the overtopping occurrence
346 by determining the correlations between *TLs* and *SWHs* (Chini and Stansby, 2012). The
347 Copula function is actually a class of function that connects joint distributions and
348 marginal distributions (Lin-Ye et al., 2016; 2017). Based on the definition of Copula
349 (Rigby and Stasinopoulos, 2005), the joint distribution of the hydrological variable pair
350 (x_1^t, x_2^t) can be described by non-stationary Copula with an explanatory variable of
351 time t :

$$352 \quad F(x_1^t, x_2^t) = C[u_1(x_1^t | \lambda_1^t), u_2(x_2^t | \lambda_2^t) | \lambda_c^t], \quad (4)$$

353 where $F(x_1^t, x_2^t)$ is the joint cumulative distribution function (*CDF*) of *TLs* and *SWHs*,
354 C represents the non-stationary Copula function, u_1 and u_2 are the non-stationary
355 cumulative marginal distribution of *TLs* and *SWHs*, with λ_1^t and λ_2^t the time-varying
356 marginal distribution parameters. If the time-dependent parameters λ_1^t , λ_2^t and λ_c^t
357 are set to constants, then Eq. (4) is converted to stationary Copula. More information
358 about the non-stationary Copula can be found in Lin-Ye et al. (2016; 2017).

359 The implementation of the time-dependent Copula is powered by the Generalized
360 Additive Model in Location, Scale and Shape (GAMLSS) package to measure the

361 partial dependence structure of the parameters (Rigby and Stasinopoulos, 2005). The
362 first step is to implement the non-stationary extreme value analysis for each variable
363 and select an appropriate marginal distribution, as presented in 3.4. Then, the
364 Archimedean Copula function is used to measure the dependence between *TLs* and
365 *SWHs* based on the well-documented Copula family methods, i.e., the Gaussian,
366 Clayton, Frank, and Gumbel (Rigby and Stasinopoulos, 2005; Lin-Ye et al., 2016). The
367 Akaike Information Criterion (AIC) values for different Copulas fitted to *TLs* and *SWHs*
368 for the periods before and after reclamation suggest that the Gaussian method is the
369 most suitable (see the Supplementary Table S2). The joint return period $T(w, s)$ is
370 formulated as:

$$371 \quad T(w, s) = \frac{1}{1 - F(w) - F(s) + F(w, s)}, \quad (5)$$

372 where $F(w)$, $F(s)$, and $F(w, s)$ are the cumulative distribution probability of *TLs*,
373 *SWHs*, and their joint distribution probability, respectively. A significant number of
374 observations are required to achieve a robust fit of the joint probability distribution, and
375 here, we used long-term simulations for this purpose.

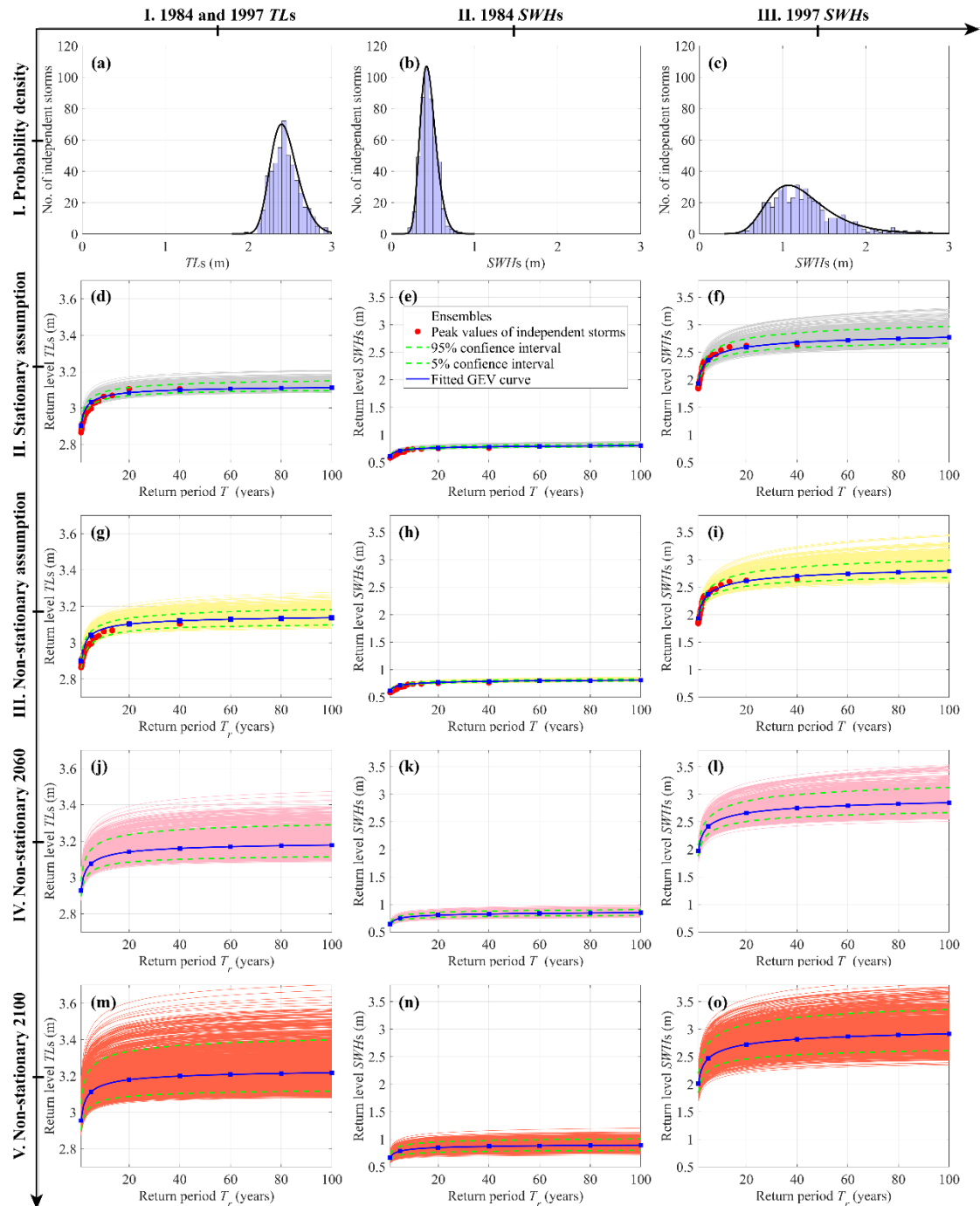
376 **4 Results**

377 **4.1 Return levels of stationary and non-stationary estimations**

378 In order to examine the changes of extreme tidal levels (*TLs*) and significant wave
379 heights (*SWHs*) due to reclamations, a detailed analysis of all independent storms is
380 provided using the plots of probability distributions (Fig. 6a-c). A more explicit
381 comparison of the change of return levels versus the corresponding return periods under
382 both stationary (ignoring the observed trend, Fig. 6d-f) and non-stationary assumptions
383 (Fig. 6g-o) are also presented. The initial goodness-of-fit of the GEV model is assessed
384 using Quantile-Quantile (Q-Q) plots of the observed and empirical values, which are
385 presented in Fig. S3 of the Supplementary. Overall, the stationary posterior probability
386 bounds of simulations do not encompass all the *TLs* points, especially for the points at
387 the beginning (Fig. 6d), indicating that the assumption of stationary model is not met,
388 considering the trend of continuous sea-level rise. Whereas, the envelope of *SWHs*
389 encloses the points of empirical return levels under both the stationary (Fig. 6e-f) and
390 non-stationary (Fig. 6 h-i) assumptions, since the trend of *SWHs* is mostly related to the
391 intensifying of typhoon storms, which is only assessed based on a relatively short period
392 of observation (e.g., 1978 - 2019). Nonetheless, if the observed linear trend continues,
393 the future predicted return levels would be inadvertently underestimated under the

394 stationary assumption. For example, considering a 100-yr-return level, it is 2.77 m
395 (stationary), 2.85 m (non-stationary of 2060), and 2.92 m (non-stationary of 2100) for
396 1997 *SWHs*; it is 3.11 m (stationary), 3.18 m (non-stationary of 2060), and 3.22 m (non-
397 stationary of 2100) for *TLs*, respectively. These results indicate that an unrepresentative
398 assumption of stationary underlying distribution would underestimate future extreme
399 return levels.

400 It is shown that the changes in the hourly *TLs* are not significant, even considering
401 the fact of reclamations between 1984 and 1997 (see Fig. S4 in the Supplementary
402 Material). The same number of *TL* histograms of independent storms, shown in Fig. 6a,
403 are observed distributing between the range of 1.8 m and 3.2 m under both 1984 and
404 1997 conditions, i.e., both median (~2.42 m) and extreme values (99.5 percentile) of
405 the *TLs* distribution are unchanged after reclamation on Fengxian Coast. In contrast,
406 the *SWHs* have increased profoundly after reclamation (Fig. 6b, c). In particular, the
407 median of *SWHs* has tripled (i.e., 0.43 m and 1.15 m for 1984 and 1997, respectively),
408 while a 145% increase in the 99.5 percentile is also observed when compared with the
409 case before reclamation, demonstrating a profound shift towards higher values of both
410 median and extreme wave height after reclamation on Fengxian Coast. In addition, the
411 return levels of 1997 *SWHs* after reclamation (Fig. 6f, i) are much higher than those
412 before reclamation in 1984 (Fig. 6e, h) under both stationary and non-stationary
413 assumptions. For example, the return levels of *SWHs* corresponding to 1-yr, 5-yr, 10-
414 yr, 20-yr, 50-yr, 100-yr and 200-yr on Fengxian Coast are increased by 1.31 (1.28 - 1.36)
415 m, 1.64 (1.60 - 1.72) m, 1.75 (1.69 - 1.85) m, 1.83 (1.76 - 1.96) m, 1.93 (1.83 - 2.08)
416 m, 1.98 (1.88 - 2.16) m and 2.02 (1.91 - 2.22) m, respectively, which corresponds to an
417 increase of *SWHs* by more than twofold when compared with the case before
418 reclamation, as presented in Supplementary Table S3. Consequently, reclamations of
419 the high marshes on Fengxian Coast had a substantial amplification of *SWHs* when
420 compared with a minor change in *TLs*.



421

422 Fig. 6. Diagnostic plot of independent storms for the probability density (1st row) and
 423 return levels vs. return periods with fitted GEV (generalized extreme value) curve (2nd
 424 - 5th row). Ensembles are used to provide the range of posterior probability bands and
 425 the confidence intervals (e.g., 5 % and 95 % quantiles). The 1st column is the tidal levels
 426 (TLs) for both 1984 and 1997 tidal flat conditions, the 2nd and 3rd columns are the
 427 significant wave heights (SWHs) under 1984 and 1997 tidal flat condition, respectively.
 428 Stationary assumption: showing the return levels under the stationary distribution
 429 function; Non-stationary assumption: exhibiting the non-stationary return levels for the

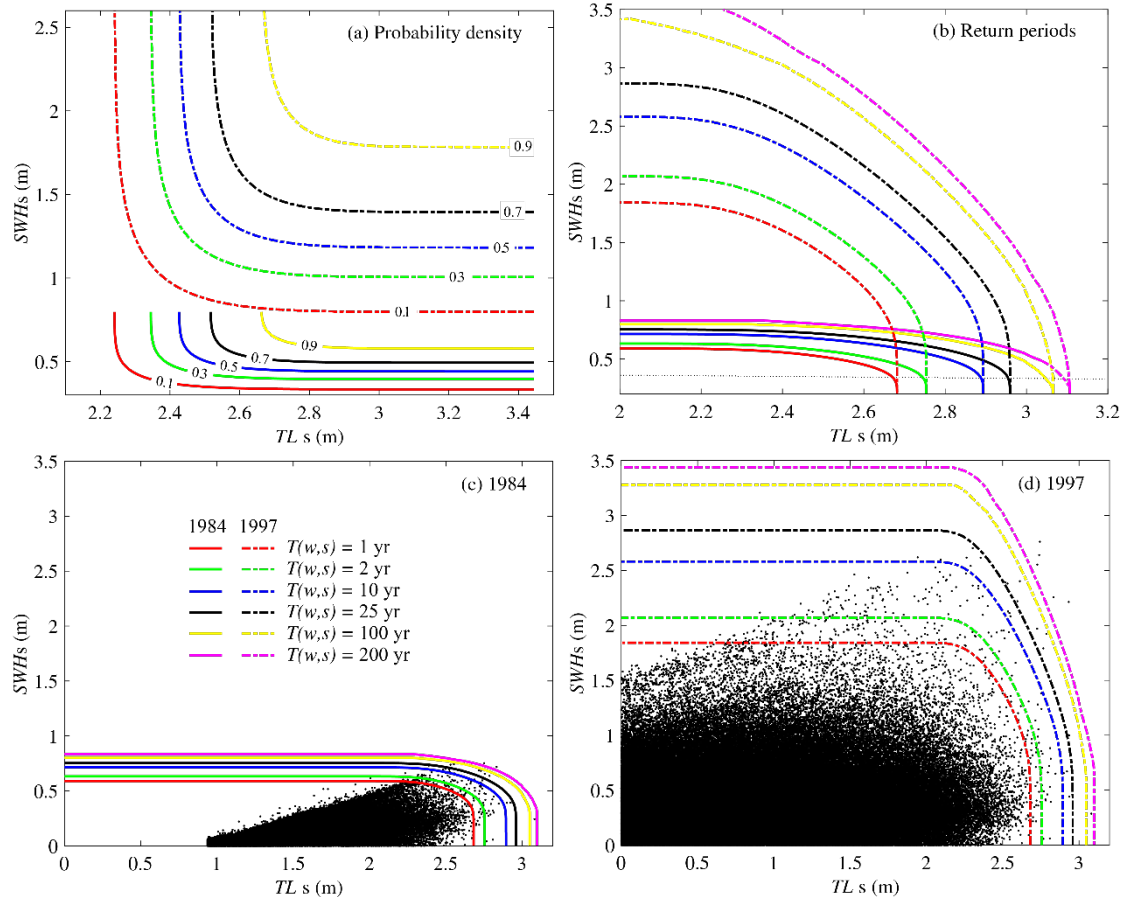
430 observation period 1979 - 2018; Non-stationary 2060: displaying the predicted non-
431 stationary return levels for 40 years beyond observations (e.g., 2019 - 2060); Non-
432 stationary 2100: displaying the predicted non-stationary return levels for 80 years
433 beyond observations (e.g., 2060 - 2100).

434 **4.2 Risk estimation based on joint probability models**

435 Based on Copulas joint probability analysis, we compared the difference in the
436 joint dependence structure of *TLs* and *SWHs* between the pre- and post-reclamation
437 periods. For the Fengxian Coast that was modified by reclamations in 1997, both
438 occurrence probabilities (Fig. 7a) and return periods (Fig. 7b) of the given *TLs* and
439 *SWHs* events tend to be more substantial for the post-reclamation period, particularly
440 for those values around the 45° line (Fig. 7a, b). Regarding the *TLs-SWHs* joint return
441 periods (Fig. 7b), different combinations of *TLs* and *SWHs* can have the same joint
442 probability of occurrence, although the overtopping volume and flood hazard may be
443 different. We also notice that, for the various return periods examined (Fig. 7b), there
444 are no obvious changes in the dependence structure between the two periods when
445 *SWHs* are lower than 0.4 m (i.e., the impacts of reclamations on the change of return
446 levels are limited for the ordinary low wind-wave conditions). On the contrary, for
447 strong wind and wave conditions higher than 0.4 m (especially for typhoons), the
448 isolines of return levels show more significant and progressive increases with the
449 decrease in *TLs* during the post-reclamation periods (Fig. 7b). These observations
450 suggest that depth-induced wave breaking during storms is absent after reclamation.
451 Consequently, the situation may become very dangerous for some typhoons even when
452 coincidence with medium-low *TL* stages.

453 The change of risk is also shown using the scatter plot of hourly *TLs* and associated
454 *SWHs*, which differs enormously between pre- and post-reclamation periods (Fig. 7c,
455 d). Though the upper right corner is influential in overtopping, it is worth noting that
456 the minimum *TLs* elevation is 0.85 m before reclamation due to the limit of tidal flat
457 elevation; the maximum wave heights show a linear increase (with a slope of 0.45) with
458 *TLs*, further demonstrating the importance of water depth on wave breaking before
459 reclamation. As a response, China has developed various design standards for sea
460 defense, depending on the properties being protected. For example, nuclear energy
461 assets are designed to be resilient to events less than 0.005%, but a typical design
462 tolerance for urban areas is a 0.5% event. For an extensive verification of this result,
463 six joint probability isolines of 100%, 50%, 10%, 4%, 1%, and 0.5% are considered

464 (Fig. 7c, d), historically known as 1 in 1, 2, 10, 25, 100 and 200-yr-return period events.
 465 Assuming the coastal defense in Shanghai is designed to withstand a 1 in 200-yr-return
 466 period event, our analyses reveal that for TL s higher than 2.8 m, for instance, to prevent
 467 wave overtopping, a dike needs to be able to withstand SWH s higher than 0.8 m and 2.4
 468 m for the periods pre- and post-reclamation, respectively. Notably, points located
 469 outside of the 200-yr-return period, in Fig. 7d, are instantaneous extreme overtopping
 470 during Typhoon 9711.



471
 472 Fig. 7. Joint cumulative probability curves and joint return period curves for nearshore
 473 TL s and SWH s. (a, b) Comparison of joint cumulative probability $F(w, s)$ curves and
 474 joint return period $T(w, s)$ curves before and after reclamation; (c, d) the scatter plot
 475 of hourly TL s- SWH s for the past 40 years, and the comparison with the associated joint
 476 return period curves under the 1984 and 1997 intertidal profiles, respectively.

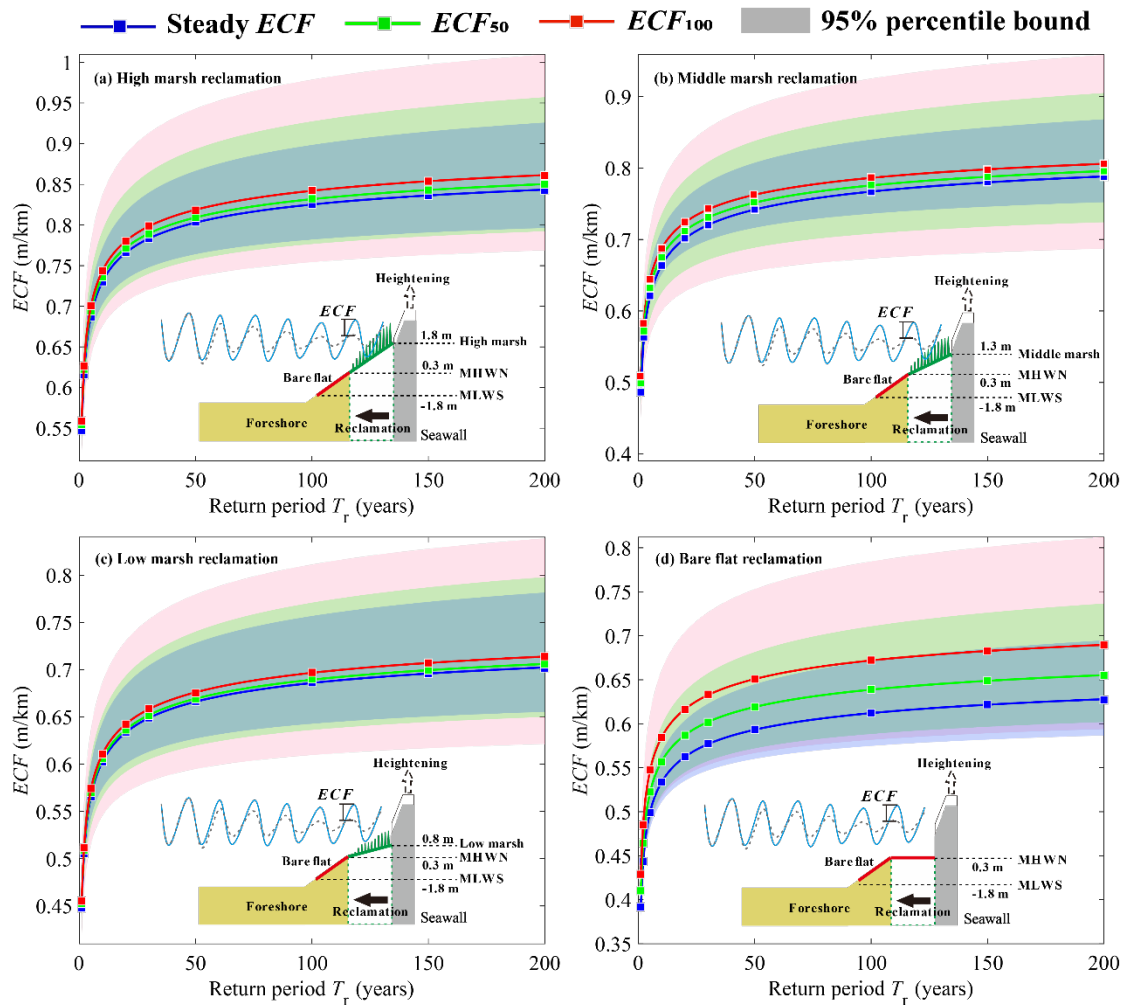
477 4.3 The conversion from tidal-flat reclamation to seawall heightening on 478 equivalent flood protection

479 The most common strategy to combat wave overtopping after reclamation of tidal-
 480 flat areas is seawall heightening. However, seawall heightening can be difficult if the
 481 intertidal subsoil is too soft to support a heavy dike. Alternatively, restoring the wide

482 tidal flat by human interventions provides a reliable way to reduce seawall overtopping
483 risks. Here, we introduce an equivalent conversion formula (ECF , m/km) to explore the
484 relationships between seawall heightening (vertical scale, in m) and tidal flat restoration
485 (horizontal scale, in km) that provides the same standard of flood protection for storms
486 of a specific return period. Firstly, we assume stationary return levels of an unbounded
487 lifetime of exceedance probability. Thus, reducing the marshes on Fengxian Coast by
488 every km width of tidal flat is estimated to increase of $SWHs$ by $ECF = 0.0536 \cdot \ln(T_r) +$
489 0.5839 m, with return periods T_r varying from 1 to 200 years (see Fig. 8a and Table S3
490 in the Supplementary Material), which is equivalent to the heightening in seawall crest
491 level to achieve the same protection ability, and vice versa. The tidal flat loss occurred
492 in 1984 is due to the reclamations of high marshes with the elevation of 1.8 m (at the
493 toe of seawall). For a general derivation, $ECFs$ of the reclamations of middle marshes
494 (elevation of 1.3 m), low marshes (elevation of 0.8 m), and bare tidal flats (elevation of
495 0.3 m) are also modeled and presented in Fig. 8b, c and d, respectively. By summarizing
496 the above four different marsh cases, a more general equation of ECF as a function of
497 tidal flat elevation (E) placed in front of the seawall can be obtained by a regression
498 model, leading to steady $ECF = 0.0493 \cdot \ln(T_r) + 0.1342 \cdot E + 0.3618$ m under stationary
499 assumption.

500 Considering the fact that the exceedance probability varies over time (Fig. 6),
501 stationary estimation assuming an unbounded lifetime of facilities will potentially
502 underestimate the risks compared with the actual lifecycle analysis. Consequently, a 50-
503 yr seawall lifecycle and 100-yr seawall lifecycle, termed as effective $ECFs$ are
504 presented in Fig. 8, which can be considered more practical estimates of future $ECFs$.
505 For example, the ECF corresponding to 100-yr-return period, reclamation of high
506 marsh is estimated to be 0.82 (0.75 - 0.89) m, 0.83 (0.77 - 0.93) m and 0.85 (0.78 - 0.98)
507 m for the unbounded lifetime, 50-yr lifecycle and 100-yr lifecycle, respectively (Fig.
508 8a). The effective $ECFs$ can be considered as a low risk (more conservative) estimation
509 of actual lifecycle analysis by taking the 95 percentiles of the $\mu(t)$ values into
510 extrapolation from historical observation to future prediction. Thus, the concept of
511 Design Life Level quantifying the probability of exceeding a fixed threshold is extended
512 to be a time-varying exceedance probability to provide a more reliable saltmarsh design.
513 Based on the non-stationary assumption the steady ECF equation is revised, leading to
514 $ECF_{50} = 0.0494 \cdot \ln(T_r) + 0.1341 \cdot E + 0.3618$ m and $ECF_{100} = 0.0495 \cdot \ln(T_r) + 0.1341 \cdot E$
515 $+ 0.3618$ m considering the seawall lifecycle of 50 years and 100 years, respectively.

516 The performance of effective ECF s are shown in Supplementary Fig. S5, where we
 517 observe a good correspondence between modeled and observed results with R^2 being
 518 0.97.

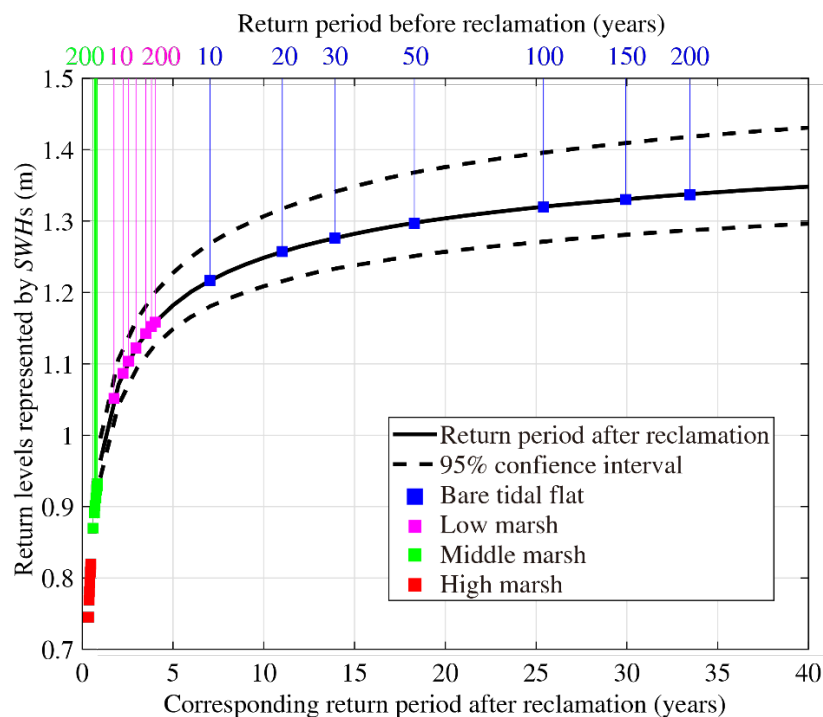


519
 520 Fig. 8. The equivalent conversion relationship (ECF) on flood protection from the
 521 heightening of seawall (in m) against 1 km reclamation of (a) the 1984 tidal flat of high
 522 marsh (1.8 m) on Fengxian Coast, considering steady ECF (the steady condition
 523 assuming an unbounded seawall lifetime), and effective ECF considering the seawall
 524 lifecycle of 50 years (ECF_{50}) and 100 years (ECF_{100}), respectively. For a general
 525 prediction, ECF for reclamations of (b) the middle marsh with the mudflat elevation of
 526 1.3 m, (c) the low marsh with the mudflat elevation of 0.8 m, and (d) the bare tidal flat
 527 with the mudflat elevation of 0.3 m are also presented, with the shade showing the 95%
 528 percentile bound.

529 4.4 Changes of occurrence probability after reclamation

530 Following wave amplification at the toe of seawall during post-reclamations, the
 531 return periods are decreased; thus, the exceedance probability of wave overtopping for

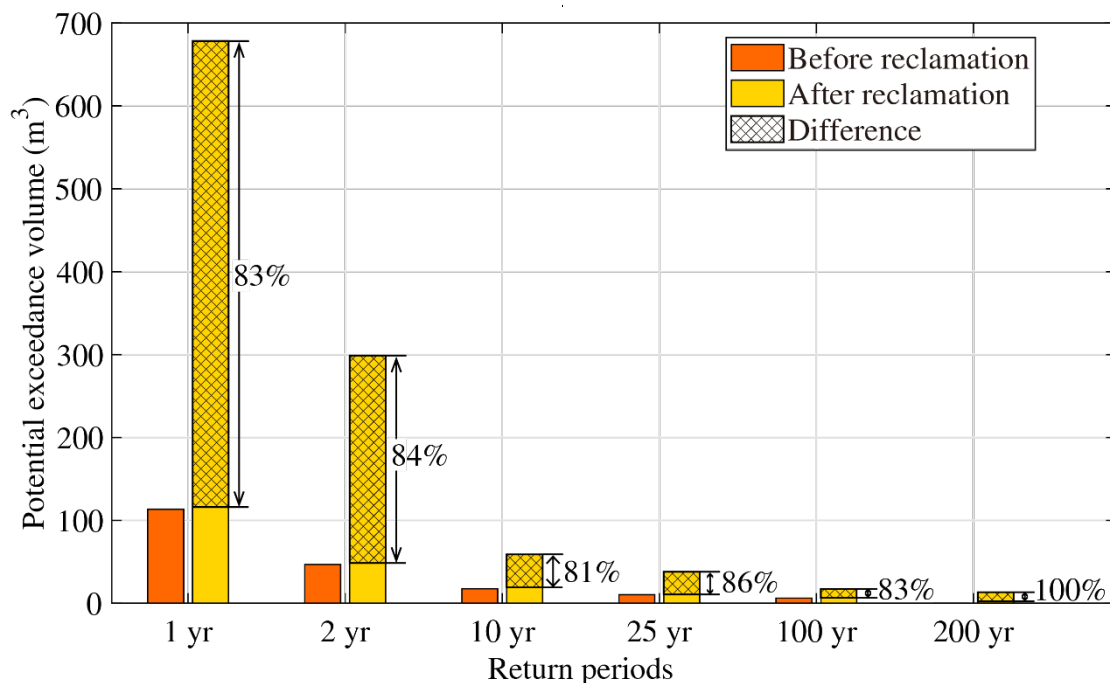
532 a given *SWHs* is also changed. Figure 9 shows how the 10 - 200 yr return periods of
 533 *SWHs* in 1984 are modified by a series of reclamations in 1997. For instance, for various
 534 elevations of tidal flat that are reclaimed assuming no improvement in seawall defense,
 535 100 - 200 yr return periods of *SWHs* would occur at least once in 25 - 35 yr for
 536 reclamations of every km width of bare tidal flat (0.3 m), at least once in 5 yr for low
 537 marshes (0.8 m), and at least once in 2 yr for middle marshes (1.3 m) or high marshes
 538 (1.8 m), respectively. Reclamations, therefore, increase the extreme magnitude of *SWHs*
 539 on the Fengxian Coast and correspondingly reduce the return period of a specific
 540 magnitude computed with the foreshore before reclamation. In other words, an
 541 exceedance probability of 0.005 - 0.01 (representative of an event that has the chance
 542 of occurrence in any given year) will increase to around 0.03 - 0.04 after reclamation
 543 of bare tidal flat, and even increase to above 0.5 for the reclamation of middle or high
 544 marshes. Thus, extreme coastal flood disasters such as the No. 9711 typhoon event
 545 would become more frequent under the present condition than those existing before the
 546 reclamation of the tidal flats on the Fengxian Coast.



547
 548 Fig. 9. Changes in return periods computed before and after reclamation of every km
 549 width of tidal marshes, where red dots, green dots, pink dots, and blue dots represent
 550 the return periods before reclamation of the high marsh, middle marsh, low marsh, and
 551 bare tidal flat, respectively. The black curve represents the return period vs. return level
 552 after reclamation, with 95% percentiles shown by dashes.

553 **4.5 The contribution of human-induced and natural changes to overtopping risks**

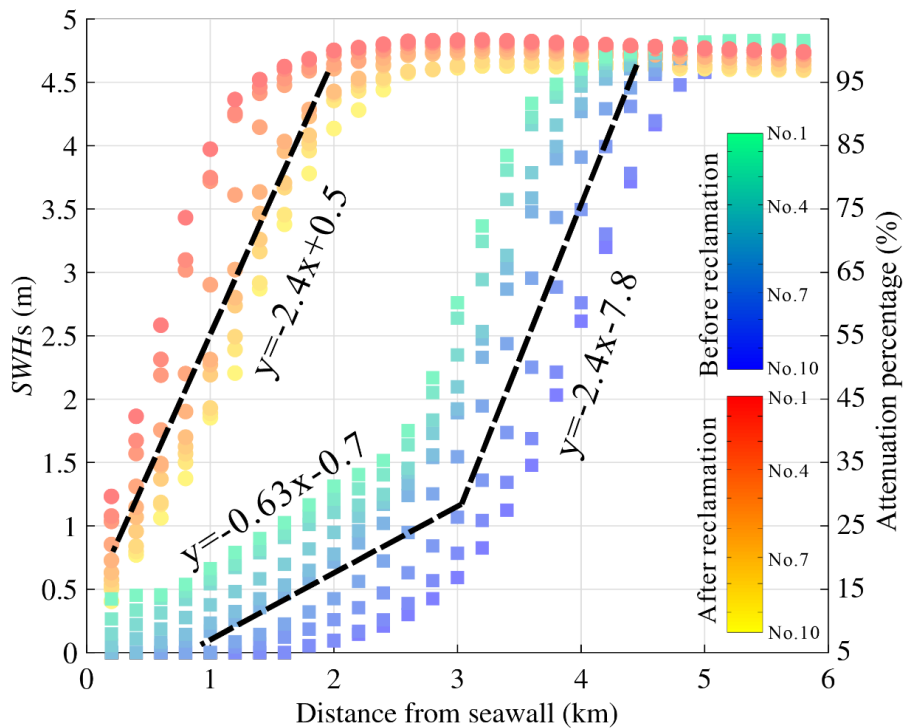
554 For any given storm wave run-ups (i.e., defined by a combination of hourly *TLs*
 555 and *SWHs* in Fig. 7c and 7d under 1984 and 1997 bathymetry, respectively) and seawall
 556 height (i.e., defined by the return levels for 1997 in Fig. 7d), we derived the total time-
 557 integrated potential exceedance volume (i.e., wave overtopping volume assuming
 558 seawall heights are set at the derived return levels) for 1984 and 1997, respectively (Fig.
 559 10). The deeper water at the toe of seawall due to tidal-flat loss caused by land
 560 reclamation increases the wave height and the potential exceedance volume as a
 561 consequence. It is shown that the increase in overtopping is more than 80% between
 562 the pre- and post-reclamation periods for the various return periods examined.
 563 Therefore, it is concluded that reclamation is a highly significant contributory factor to
 564 the storm overtopping of historical events such as Typhoon No. 9711, and it is estimated
 565 that human-induced and natural changes had contributed approximately 80% and 20%
 566 to storm overtopping of typhoon disasters, respectively, during post reclamations. To
 567 avert such an event, the seawall height would need to have been raised as part of the
 568 intertidal reclamation procedure, in line with the increase in wave conditions suggested
 569 by the *ECF*, to produce an equivalent protection standard.
 570



571
 572 Fig. 10. Comparison of potential exceedance volume before and after reclamation,
 573 assuming seawall is set to the heights of 1 in 1, 2, 10, 25, 100, and 200-yr-return levels
 574 computed with 1997 narrow intertidal condition.

575 **4.6 Wave attenuation by tidal flat**

576 Tidal flat forms an interface between land and sea, which dissipates wave energy,
 577 thereby reducing the impact of storms on the coastal area. Hindcasting the ten most
 578 influential storms occurred over the last 40 years (i.e., Typhoon 7910, 8114, 9711, 0012,
 579 0509, 0608, 0813, 1211, 1323, and 1416), based on pre- and post-reclamation
 580 bathymetries, demonstrates that the shallow tidal flats indeed strongly attenuate wave
 581 propagation towards shore (Fig. 11). Before reclamation, the *SWHs* are initially
 582 decreased by an average of 2.4 m per km for a sudden morphology transition from the
 583 deep bay (4.5 km offshore at around -9 m depth) to the shallow coast (see Fig. 2a and
 584 Fig. 11), and is further attenuated by 1.2 m when the waves passed over the additional
 585 3 km wide tidal flat, transition from the depth of -3.5 m to the toe of the original seawall
 586 in 1984. The additional (secondary) wave attenuation after the major wave dissipation
 587 is due to the existence of extensive high-marsh tidal flat. However, after reclamation,
 588 the high-marsh tidal flat is completely lost, so as the secondary wave attenuation as a
 589 consequence. The *SWHs* are monotonically reduced from a maximum height of
 590 approximately 4.5 m to the height of 1 m over a distance of 1.5 km (i.e., equivalent to
 591 a linear slope of 2.4 m per km). Therefore, wave reductions are strongly related to width
 592 and elevation of the intertidal flat.



593
 594 Fig. 11. Trend analysis of wave height reduction and attenuation ratio for the ten largest
 595 storms during the past 40 years. Colorbars denote the conditions before and after
 596 reclamation.

597 **5 Discussion**

598 Although vegetated foreshore is demonstrated to provide storm protection (Möller
599 et al., 2014; Reed et al., 2018), it is proved challenging to quantify the evidence of the
600 impacts of the tidal flat reclamation program on coastal flood risks due to the facts that
601 (i) intertidal reclamations are always accompanied with procedures of seawall
602 strengthening and heightening, (ii) tidal flat morphology consisting of a sediment body
603 in front of the dike is continuously evolving especially shortly after reclamation, and
604 (iii) it is difficult to establish to what the extent and severity the overtopping may have
605 occurred had the intertidal reclamation not been implemented. We address these
606 challenges by (i) analyzing the potential exceedance probability assuming the seawall
607 height set to the obtained return levels rather than using the actual seawall height, (ii)
608 modeling the past extreme events to identify the impacts of reclamations, and (iii)
609 comparing the possibility of overtopping that could have occurred had the reclamation
610 not been implemented. Specifically, a cascade of numerical models has been designed
611 to transfer the regional surge propagation to local wave overtopping. This framework
612 is coupled with a time-dependent extreme value analysis to investigate the long-term
613 influence of tidal flat reclamations.

614 **5.1 The impacts of coastal reclamations on risk aggravating**

615 Reclamation of the tidal flat profoundly influenced the coastal geomorphology,
616 and thus, increased wave run-ups (Loder et al., 2009; Liu et al., 2019). The derivation
617 of *ECFs* demonstrates that a lower intertidal elevation with a steep gradient profile after
618 reclamation could allow more substantial overtopping than the foreshore before
619 reclamation, and this conversion relationship positively correlated with foreshore
620 elevations and slopes at the toe of the seawall (Salaudhin and Pearson, 2019). In
621 addition, the increase in wave height due to tidal flat reclamation could potentially
622 increase direct wave attacks on the otherwise protected seawall, exacerbating damages
623 and increasing the need for reinforcement (Loder et al., 2009; Vuik et al., 2016).
624 Erosion of soil at the toe of the seawall after reclamation may also occur during storm
625 events, increasing the need for armoring the intertidal morphology (Loder et al., 2009).
626 Recently, breakwaters had been placed at the wet-side of seawall around Fengxian
627 Coast to protect against wave run-ups (see Supplementary Fig. S6). This is consistent
628 with the results of Chini and Stansby (2012) for coastlines not protected by nearshore
629 sandbanks, while for coasts with fast accretion, reclamation has a potentially lower
630 impact on the amplification of nearshore waves and therefore overtopping risks (e.g.,

631 in the vicinity of Nanhui on the southeast coast of Shanghai, see Fig. 1b) (Zhang et al.,
632 2018b).

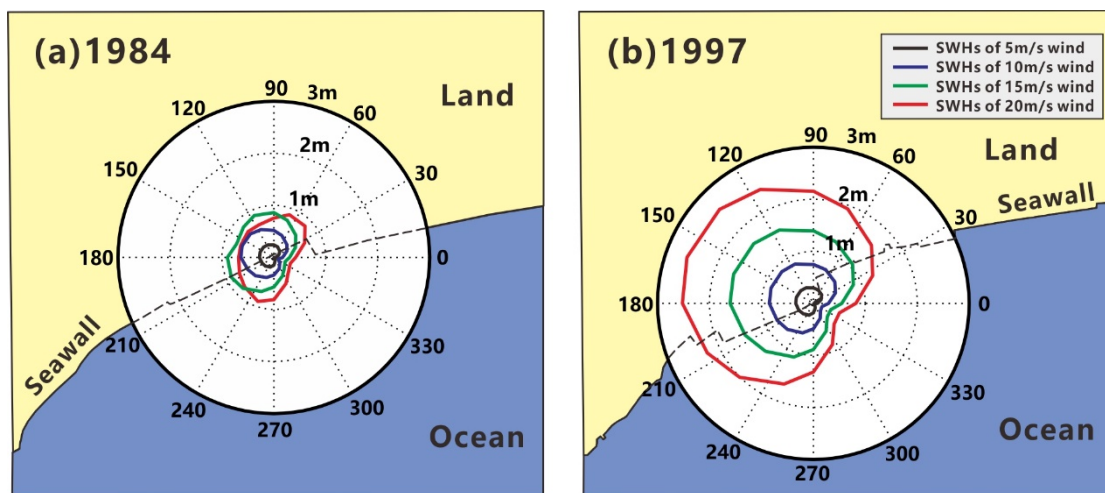
633 Intertidal conservations, on the other hand, can effectively mitigate overtopping
634 by limiting the transfer of offshore wind-waves to coastal wave run-ups (Bi et al., 2012;
635 Vuik et al., 2016). Möller et al. (1999; 2014) presented quantitative evidences for wave
636 attenuation by coastal saltmarshes over a wide range of tidal and meteorological
637 conditions both numerically and experimentally. The increases in bottom friction and
638 bulk drag force by vegetation are the primary reasons for wave attenuation over the
639 saltmarshes (Möller et al., 1999; Vuik et al., 2016). Here, the effect of the bulk drag
640 force is neglected to provide a more conservative estimation. It is predicted that restore
641 in every km width of tidal flat corresponds to approximate the asymptote of $ECF =$
642 $0.0493 \cdot \ln(T_T) + 0.1342 \cdot E + 0.3618$ m rise of seawall height on the equivalent flood
643 protection (Fig. 8). Nevertheless, changes in sedimentation affect intertidal
644 conservation, and this may vary over space and time, e.g., for rapidly regression area
645 near the mouth of Ganges estuary and Yellow River estuary (Adnan et al., 2019;
646 Temmerman et al., 2013; Barbier, 2015), or transgression foreshores near Pearl River
647 estuary and Hong estuary (Kundzewicz et al., 2019; Liu et al., 2019), but delivers a
648 consistent role of tidal flats for coastal protection on the contribution to wave
649 attenuation. Therefore, it is suggested that wide tidal flat should be restored in front of
650 dikes via human interventions in the face of rising sea levels and intensified storms
651 (Kirwan et al., 2016). Otherwise, the seawall height would need to have been raised as
652 part of the intertidal reclamation procedure (Liu et al., 2019), in line with the increase
653 in wave conditions suggested by the equivalent conversion relationship.

654 **5.2 The sensitivity of *SWHs* dynamics to wind force**

655 In order to quantitatively explain the reason of overtopping risk variation after
656 reclamation, a sensitivity test of the wave propagation towards the toe of seawall is
657 compared with varying wind forces under both 1984 and 1997 bathymetries (Fig. 12).
658 Obviously, the wave rose shows three-fivefold larger the magnitude of *SWHs* after
659 reclamation than that before reclamation, which should have schematically
660 demonstrated the causes of the increase in extreme wave height. A significant change
661 in *SWHs* is also observed when the wind speed changes ranging 5 - 20 m/s and wind
662 direction changes ranging 0 - 360°. The results are consistent with those from Tuan and
663 Oumeraci (2010) and the manual of EurOtop (2018), which suggests that *SWHs*
664 increase with the increase in wind speed but decrease with the incidence of wind shifts

665 away from the angle normal to the coastline. Therefore, except for wind speed, wind
666 incidence is also a critical parameter impacting wave heights at the toe of the seawall
667 because wave run-ups on the outer slope of the seawall are governed by both wave
668 periods and directions (Loder et al., 2009; Altomare et al., 2016; EurOtop, 2018).

669 In addition, the shoreward winds are shown to be more influential than offshore
670 winds on wave generation (Fig. 12). Since the prevailing seasonal winds in eastern
671 China vary in the southeast-northwest direction during summer and winter, respectively
672 (Fig. 4b, c, see also Zhang et al., 2018a), indicating higher wind-waves during summer
673 (the typhoon season) than those during winter near Fengxian Coast (Zhang et al., 2018a).
674 Notably, before reclamation in 1984, the wide and shallow intertidal is very efficient at
675 reducing *SWHs* when the wind angle is normal to the coastline at high wind speed. A
676 maximum *SWHs* reduction rate of 35% is observed when the wind speed is 20 m/s and
677 the wind incidence is normal to the coastline. Therefore, it is predictable that before
678 reclamation in 1984, the wide and shallow tidal flats could protect the coastline by
679 reducing the most severe wind-waves during the worst typhoon conditions.
680 Nevertheless, this function is totally lost after reclamation, which generally agrees with
681 the wave attenuating measurements reported in other literatures (Loder et al., 2009;
682 Vuik et al., 2016; Willemsen et al., 2020).



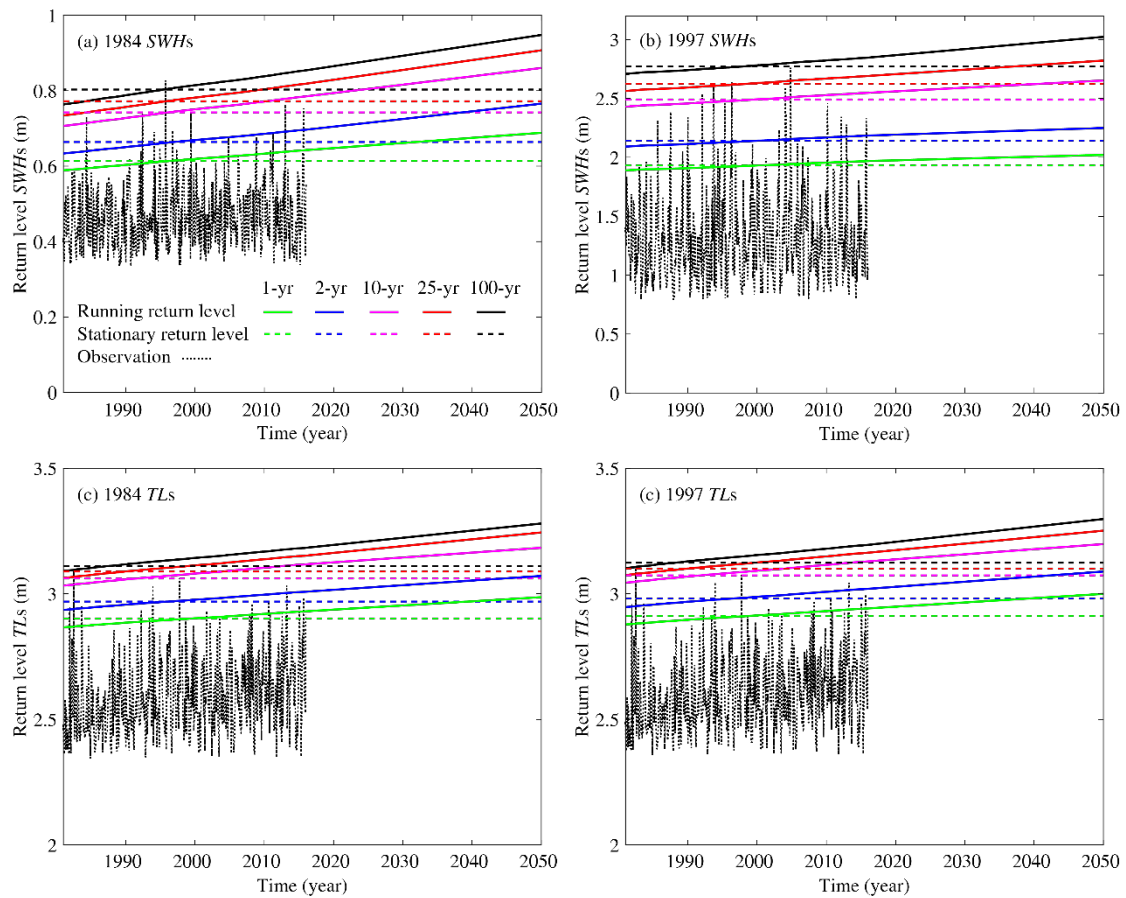
683
684 Fig. 12. Sensitivity tests of wave propagation approaching the toe of the seawall. (a)
685 Directional wave rose under the applied morphological profiles of 1984 and (b) under
686 the 1997 tidal flat profile. The magnitude of *SWHs* changes following the change of
687 both wind direction ($0^\circ - 360^\circ$) and wind speed (5 - 20 m/s). The sectors indicate the
688 wave directions, or the direction towards which the wind vector is directed.

689 5.3 Contribution to coastal flood defense designs

690 Coastal defense design has long relied on stationary return levels, assuming the
691 constant occurrence probability of extreme event over time (Altomare et al., 2016;
692 Rootzén and Katz, 2013). However, substantial evidences show that the climate is non-
693 stationary, so as the associated hydrologic extremes, possibly due to both anthropogenic
694 and natural changes (Barbier, 2015; Cheng et al., 2014). Therefore, the concept of
695 Design Life Level, introduced by Rootzén and Katz (2013), quantifies the probability
696 of exceeding a fixed threshold during the design life of seawall should be improved to
697 meet the non-stationary purpose. We assume the location parameter (μ) of the
698 underlying distribution function is time-dependent (Rigby and Stasinopoulos, 2005;
699 Lin-Ye et al., 2016; 2017) and hence, the extreme value of the distribution varies with
700 time (Cheng et al., 2014). A visual inspection indicates an upward trend for *WLs* and
701 *SWHs* during observations (Fig. 13), which is confirmed with the Mann-Kendall trend
702 test at the 5% significance level. Figure 13 shows how the running return level varies
703 with the time covariate used in the linear trend assumption (Eq. 2). This means that the
704 return levels vary with time to keep the occurrence probability of an extremal event
705 constant, such that a specific return level used for all years have the same risk.

706 On Fengxian Coast, both *WLs* and *SWHs* show linear running return levels
707 increase over time (Fig. 13), which confirms the aggravation of future overtopping of a
708 specific return level, assuming no improvement in the seawall defense. On the other
709 hand, *TLs* show little change after reclamation while *SWHs* are almost tripled; thus,
710 extreme typhoon events will become more frequent than those existing before
711 reclamation. The *ECF* demonstrating the relationship between tidal flat loss and seawall
712 heightening, illustrated in Fig. 8, provides suitable guidance for seawall redesign. The
713 minor changes in *TLs* demonstrate that reclamations in a local-scale at nearshore
714 imposed a limited influence on the large-scale tidal state, which is mainly controlled by
715 astronomical tide and swell propagation from the open sea (Loder et al., 2009;
716 Niroomandi et al., 2018; Zhang et al., 2018a). It is worth noting that extrapolating the
717 historical trends linearly into the future implies that the characteristics of the past trend
718 continues following an inertia (linear function) without constraints, which might be not
719 realistic (Méndez et al., 2006; Cheng et al., 2014). For time-varying prediction of the
720 probability of exceedance instead of simply linear extrapolating result from historical
721 trends, one must rely on other tools like numerical modeling, as the dynamical Yangtze-
722 Hangzhou Bay simulations performed in this study. In principle, long-term and reliable
723 future boundary conditions of atmosphere (e.g., typhoons) and hydrology (e.g., SLRs)

724 should be addressed appropriately of the first importance. Therefore, care should be
 725 taken in the future earth prediction, especially for the long-term climate changes (Shi
 726 et al., 2000; Dee et al., 2011).



727
 728 Fig. 13. Comparison of the running and stationary return levels before and after
 729 reclamation used for all years in coastal flood defense design.

730 5.4 Implications for coastal reclamation adaptations

731 Large-scale reclamations and embankments have been implemented in the coastal
 732 zone of Shanghai for more than half a century (Xie et al., 2017). The reclamation
 733 procedure is still underway and looks set to continue (Zhang et al., 2019). The most
 734 straightforward engineering approach in response to the aggravating of coastal flood
 735 hazards due to tidal flat loss is seawall heightening. However, seawalls and dikes only
 736 provide flood protection to a given hazard severity (EurOtop, 2018; Tuan and Oumeraci,
 737 2010). These structures are typically costly and may exacerbate flooding due to the
 738 build-up of wave run-ups (Altomare et al., 2016; Kundzewicz et al., 2019). Moreover,
 739 the base subsidence will further lower the seawall's protection standard if maintenance
 740 is inadequate, and therefore, potentially aggravate the overtopping risks (Temmerman
 741 et al., 2013). There are reported examples worldwide of protection failure by traditional

742 hard engineering defenses, e.g., North Sea storm surge flood in 1953, Typhoon Winnie
743 flood in 1997, Hurricane Katrina flood in 2005, Storm Xynthia flood in 2010, and most
744 recently, Typhoon Mangkhut flood in 2018. Alternative adaptation strategies, such as
745 vegetated foreshore, sediment nourishment, and groynes should be considered part of
746 the Flood Defense Safety Plan by building the hybrid seawall-foreshore system to
747 maximize the coastal resilience functions.

748 Generally, wide foreshore restorations in front of seawall via human interventions
749 are both for the immediate wave run-up reduction (Reed et al., 2018; Vuik et al., 2019)
750 and in anticipation of elevated future risks due to SLR (Temmerman et al., 2013). On
751 the other hand, saltmarshes on the foreshores are a gift of nature, and they provide
752 valuable ecosystem services that hard seawalls do not (Bouma et al., 2010; Reed et al.,
753 2018). The comparison of overtopping changes and *ECF* estimation before and after
754 reclamation reported in this study should help to demonstrate the importance of tidal
755 flats on flood mitigation and to establish plans to adapt coastal zone against flood
756 hazards by helping to optimize protection design and maximize the benefit of flood
757 management. Nevertheless, the usability of such a nature-based solution should fit in
758 with the surrounding physical environment (Adnan et al., 2019; Vuik et al., 2019),
759 especially for Fengxian coastal area, where the foreshore has evolved from
760 accumulating to eroding recently (Xie et al., 2017). Therefore, an assessment of
761 sediment availability, technical feasibility, and long-term influence on landscape
762 evolution is required before implementing the nature-based solution.

763 Although building with nature for flood protection is more challenging and
764 effortful than seawall heightening (Vuik et al., 2016; 2018), the multiple benefits of
765 flood mitigation and high ecological values could potentially be improved by designing
766 hybrid foreshore-seawall systems via human foreshore restoration activities (Möller et
767 al., 2014). This technique could be applied to other estuaries and coasts worldwide,
768 especially for developing countries of emerging economies heavily dependent on
769 intertidal reclamations (Temmerman et al., 2013; Barbier, 2015). Examples of the
770 potential applications are the Pearl River Delta in China, the Ganges Delta in
771 Bangladesh, the Manila Estuary Delta in the Philippines, and the Mekong Delta in
772 Vietnam, where the low-lying deltas are vulnerable to typhoon impacts, thus the hybrid
773 solution is more attractive.

774 **6 Conclusions**

775 With coastal reclamations, tidal flats are lost, while wave run-ups at the toe of the

776 seawall are increased, threatening the sustainability of coastal development around
777 Shanghai. As a safety measure to protect against flooding, seawall management requires
778 a derivation of the quantitative relationship between tidal flat loss and the increase in
779 extreme events intensity. The results show that the intertidal reclamations are the
780 primary source of increased flood risks in locations dominated by wind waves, with
781 both wind speed and wind direction being the essential driving factors. In particular,
782 wind waves pose the highest flood hazard when wind speeds are the most extreme, and
783 the wind direction is normal to the coastline. While reclamation and embankments have
784 protected against extreme tidal water levels and storm surges of moderate severity on
785 the Fengxian Coast, they have exacerbated more serious the wave run-ups of the seawall,
786 and promote potential severe wave overtopping disasters when coincidence with the
787 extreme storm surges. Tidal flat reclamation, therefore, aggravates the risk from storms
788 and increases the frequency of occurrence of a given rate. It is concluded that the
789 disasters of coastal flooding after the reclamation of 1997 in Hangzhou Bay are a result
790 of both anthropogenic and natural activities.

791 The construction of the seawall-foreshore hybrid system is more sustainable and
792 cost-effective than the conventional hard engineering defense. Although the practice of
793 conventional defense design is well established, and few natural systems can eliminate
794 all risks, these environmental approaches could potentially make a meaningful
795 contribution. Where this function exists, its wave mitigation ability could be customized
796 to enhance flood defense by the integration with conventional approaches, maximizing
797 the system's contribution to flood protection. Understanding the effect of tidal flats on
798 coastal protection under storm conditions is of utmost importance to determine the
799 design criteria for hybrid flood defense systems of a seawall shielded by sufficient tidal
800 flats as suggested by our proposed *ECF* relationship. This equivalent conversion
801 relationship on flood protection may be relevant to other storm-impacted coastlines
802 worldwide that are subject to large-scale reclamations.

803 **Acknowledgments**

804 This research is supported by the National Natural Science Foundation of China
805 (Project no.: 41701001, 2018YFE0109900, 51761135024), China Postdoctoral Science
806 Foundation (Project no.: 2018M630414) and Guangdong Provincial Department of
807 Science and Technology (2019ZT08G090). The authors would like to thank Dr. Elisa
808 Ragno and Prof. Oswaldo Morales Napoles from Delft University of Technology for
809 their helps on non-stationary Copulas. Great thanks are due to the reviewers for a

810 number of very constructive comments and suggestions that have helped the substantial
811 improvement of the manuscript.

812

813 **References:**

814 Adnan, M.S.G., Haque, A. and Hall, J.W., 2019. Have coastal embankments reduced
815 flooding in Bangladesh? *Science of The Total Environment* 682, 405-416.

816 Altomare, C., Suzuki, T., Chen, X., Verwaest, T. and Kortenhuis, A., 2016. Wave
817 overtopping of sea dikes with very shallow foreshores. *Coastal Engineering* 116, 236-
818 257.

819 Barbier, E.B., 2015. Climate change impacts on rural poverty in low-elevation coastal
820 zones. *Estuarine Coastal and Shelf Science* 165, A1-A13.

821 Bi, X., Liu, F. and Pan, X., 2012. Coastal projects in China: From reclamation to
822 restoration. *Environmental Science & Technology* 46(9), 4691-4692.

823 Bouma, T.J., van Belzen, J., Balke, T., Zhu, Z., Airoidi, L., Blight, A.J., Davies, A.J.,
824 Galvan, C., Hawkins, S.J., Hoggart, S.P.G., Lara, J.L., Losada, I.J., Maza, M.,
825 Ondiviela, B., Skov, M.W., Strain, E.M., Thompson, R.C., Yang, S., Zanuttigh, B.,
826 Zhang, L. and Herman, P.M.J., 2014. Identifying knowledge gaps hampering
827 application of intertidal habitats in coastal protection: Opportunities & steps to take.
828 *Coastal Engineering* 87, 147-157.

829 Bouma, T. J., Vries, M. B. D., Low, E., Kusters, L., Herman, P. M. J., Táncoz, I. C.,
830 Temmerman, S., Hesselink, A., Meire, P. and Regenmortel, S. V., 2005. Flow
831 hydrodynamics on a mudflat and in salt marsh vegetation: identifying general
832 relationships for habitat characterisations. *Hydrobiologia* 540(1), 259-274.

833 Bouma, T.J., Vries, M.B.D. and Herman, P.M.J., 2010. Comparing ecosystem
834 engineering efficiency of two plant species with contrasting growth strategies. *Ecology*
835 91(9), 2696-2704.

836 Cheng, L., AghaKouchak, A., Gilleland, E. and Katz, R.W., 2014. Non-stationary
837 extreme value analysis in a changing climate. *Climatic Change* 127(2), 353-369.

838 Chini, N. and Stansby, P.K., 2012. Extreme values of coastal wave overtopping
839 accounting for climate change and sea level rise. *Coastal Engineering* 65, 27-37.

840 Dee, D.P., Uppala, S.M., Simmons, A.J., Berrisford, P., Poli, P., Kobayashi, S., Andrae,
841 U., Balmaseda, M.A., Balsamo, G., Bauer, P., Bechtold, P., Beljaars, A.C.M., van de
842 Berg, L., Bidlot, J., Bormann, N., Delsol, C., Dragani, R., Fuentes, M., Geer, A.J.,
843 Haimberger, L., Healy, S.B., Hersbach, H., Hólm, E.V., Isaksen, L., Kållberg, P.,

844 Köhler, M., Matricardi, M., McNally, A.P., Monge-Sanz, B.M., Morcrette, J.J., Park,
845 B.K., Peubey, C., de Rosnay, P., Tavolato, C., Thépaut, J.N. and Vitart, F., 2011. The
846 ERA-Interim reanalysis: configuration and performance of the data assimilation system.
847 Quarterly Journal of the Royal Meteorological Society 137(656), 553-597.

848 EDF, R.D.S., 2011. TOMAWAC software for sea state modelling on unstructured grids
849 over oceans and coastal seas. Release 6.1. France, EDF R&D.

850 EurOtop, 2018. Manual on wave overtopping of sea defences and related structures: An
851 overtopping manual largely based on European research, but for worldwide application.
852 <http://www.overtopping-manual.com/eurotop/downloads/>.

853 Janin, J.M., Lepeintre, F. and Péchon, P., 1992. TELEMAC-3D: A finite element code
854 to solve 3D free surface flow problems. Springer. 489-506 pp.

855 Kirwan, M.L., Temmerman, S., Skeeahan, E.E., Guntenspergen, G.R. and Fagherazzi,
856 S., 2016. Overestimation of marsh vulnerability to sea level rise. Nature Climate
857 Change 6, 253.

858 Kundzewicz, Z. W., Su, B., Wang, Y., Xia, J., Huang, J. and Jiang, T., 2019. Flood risk
859 and its reduction in China. Advances in Water Resources 130, 37-45.

860 Lin-Ye, J., García-León, M., Gràcia, V., Ortego, M.I., Lionello, P. and Sánchez-Arcilla,
861 A., 2017. Multivariate statistical modelling of future marine storms. Applied Ocean
862 Research 65, 192-205.

863 Lin-Ye, J., Garcia-Leon, M., Gracia, V. and Sanchez-Arcilla, A., 2016. A multivariate
864 statistical model of extreme events: an application to the catalan coast. Coastal
865 Engineering 117, 138-156.

866 Liu, X., Wang, Y., Costanza, R., Kubiszewski, I., Xu, N., Yuan, M. and Geng, R., 2019.
867 The value of China's coastal wetlands and seawalls for storm protection. Ecosystem
868 Services 36, 100905.

869 Loder, N.M., Irish, J.L., Cialone, M.A. and Wamsley, T.V., 2009. Sensitivity of
870 hurricane surge to morphological parameters of coastal wetlands. Estuarine, Coastal
871 and Shelf Science 84(4), 625-636.

872 Méndez, F.J., Menéndez, M., Luceño, A. and Losada, I.J., 2006. Estimation of the long-
873 term variability of extreme significant wave height using a time-dependent Peak Over
874 Threshold (POT) model. Journal of Geophysical Research: Oceans 111, C07024.

875 Menéndez, P., Losada, I. J., Beck, M. W., Torres-Ortega, S., Espejo, A., Narayan, S.,
876 Díaz-Simal, P. and Lange, G., 2018. Valuing the protection services of mangroves at
877 national scale: The Philippines. Ecosystem Services 34, 24-36.

878 Möller, I., Kudella, M., Rupprecht, F., Spencer, T., Paul, M., van Wesenbeeck, B. K.,
879 Wolters, G., Jensen, K., Bouma, T. J., Miranda-Lange, M., and Schimmels, S., 2014.
880 Wave attenuation over coastal salt marshes under storm surge conditions. *Nature*
881 *Geoscience* 7(10), 727-731.

882 Möller, I., Spencer, T., French, J.R., Leggett, D.J. and Dixon, M., 1999. Wave
883 transformation over salt marshes: a field and numerical modelling study from north
884 Norfolk, England. *Estuarine, Coastal and Shelf Science* 49(3), 411-426.

885 Niroomandi, A., Ma, G., Ye, X., Lou, S. and Xue, P., 2018. Extreme value analysis of
886 wave climate in Chesapeake Bay. *Ocean Engineering* 159, 22-36.

887 Reed, D., van Wesenbeeck, B., Herman, P.M.J. and Meselhe, E., 2018. Tidal flat-
888 wetland systems as flood defenses: Understanding biogeomorphic controls. *Estuarine,*
889 *Coastal and Shelf Science* 213, 269-282.

890 Rigby, R.A. and Stasinopoulos, D.M., 2005. Generalized additive models for location,
891 scale and shape. *Journal of the Royal Statistical Society: Series C (Applied Statistics)*
892 54(3), 507-554.

893 Rootzén, H. and Katz, R.W., 2013. Design life level: quantifying risk in a changing
894 climate. *Water Resources Research* 49(9), 5964-5972.

895 Salauddin, M. and Pearson, J.M., 2019. Wave overtopping and toe scouring at a plain
896 vertical seawall with shingle foreshore: a physical model study. *Ocean Engineering* 171,
897 286-299.

898 Shi, Y., Zhu, J., Xie, Z., Ji, Z., Jiang, Z. and Yang, G., 2000. Prediction and prevention
899 of the impacts of sea level rise on the Yangtze River Delta and its adjacent areas.
900 *Science in China Series D-Earth Sciences* 43(4), 412-422.

901 Temmerman, S., Meire, P., Bouma, T. J., Herman, P. M. J., Ysebaert, T. and De Vriend,
902 H. J., 2013. Ecosystem-based coastal defence in the face of global change. *Nature*
903 504(7478), 79-83.

904 Tuan, T.Q. and Oumeraci, H., 2010. A numerical model of wave overtopping on
905 seadikes. *Coastal Engineering* 57(8), 757-772.

906 Vuik, V., Borsje, B.W., Willemsen, P.W.J.M. and Jonkman, S.N., 2019. Salt marshes
907 for flood risk reduction: Quantifying long-term effectiveness and life-cycle costs.
908 *Ocean & Coastal Management* 171, 96-110.

909 Vuik, V., Jonkman, S.N., Borsje, B.W. and Suzuki, T., 2016. Nature-based flood
910 protection: The efficiency of vegetated foreshores for reducing wave loads on coastal
911 dikes. *Coastal Engineering* 116, 42-56.

912 Vuik, V., Suh Heo, H.Y., Zhu, Z., Borsje, B.W. and Jonkman, S.N., 2018. Stem
913 breakage of salt marsh vegetation under wave forcing: A field and model study.
914 *Estuarine, Coastal and Shelf Science* 200, 41-58.

915 Wang, J., Gao, W., Xu, S. and Yu, L., 2012. Evaluation of the combined risk of sea
916 level rise, land subsidence, and storm surges on the coastal areas of Shanghai, China.
917 *Climatic Change* 115(3-4), 537-558.

918 Wang, L., Zhang, M., Wen, J., Chong, Z., Ye, Q. and Ke, Q., 2019. Simulation of
919 extreme compound coastal flooding in Shanghai. *Advances in Water Science* 30(4),
920 546-555.

921 Willemsen, P.W.J.M., Borsje, B.W., Vuik, V., Bouma, T.J. and Hulscher, S.J.M.H.,
922 2020. Field-based decadal wave attenuating capacity of combined tidal flats and salt
923 marshes. *Coastal Engineering* 156, 103628.

924 Xie, D., Pan, C., Wu, X., Gao, S. and Wang, Z.B., 2017. Local human activities
925 overwhelm decreased sediment supply from the Changjiang River: Continued rapid
926 accumulation in the Hangzhou Bay-Qiantang Estuary system. *Marine Geology* 392, 66-
927 77.

928 Zhang, M., Townend, I., Cai, H., He, J. and Mei, X., 2018a. The influence of seasonal
929 climate on the morphology of the mouth-bar in the Yangtze Estuary, China. *Continental*
930 *Shelf Research* 153(Supplement C), 30-49.

931 Zhang, M., Townend, I., Zhou, Y., Wang, L. and Dai, Z., 2019. An examination of
932 estuary stability in response to human interventions in the South Branch of the Yangtze
933 (Changjiang) estuary, China. *Estuarine, Coastal and Shelf Science* 228, 106383.

934 Zhang, X., Zhang, Y., Zhu, L., Chi, W., Yang, Z., Wang, B., Lv, K., Wang, H. and Lu,
935 Z., 2018b. Spatial-temporal evolution of the eastern Nanhui mudflat in the Changjiang
936 (Yangtze River) Estuary under intensified human activities. *Geomorphology* 309, 38-
937 50.

938